AD_________________

Award Number: DAMD17-99-1-9121

TITLE: Improved MR Images of Breast Lesions with Fast Spectroscopic Imaging

PRINCIPAL INVESTIGATOR: Gregory S. Karczmar, Ph.D.

CONTRACTING ORGANIZATION: The University of Chicago
Chicago, IL 60637

REPORT DATE: October 2003

TYPE OF REPORT: Final

PREPARED FOR: U.S. Army Medical Research and Materiel Command
Fort Detrick, Maryland 21702-5012

DISTRIBUTION STATEMENT: Approved for Public Release;
Distribution Unlimited

REPORT DOCUMENTATION PAGE

Form Approved
OMB No. 074-0188

1. AGENCY USE ONLY (Leave blank)	**2. REPORT DATE** October 2003	**3. REPORT TYPE AND DATES COVERED** Final (15 Sep 1999 - 14 Sep 2003)

4. TITLE AND SUBTITLE
Improved MR Images of Breast Lesions with Fast Spectroscopic Imaging

5. FUNDING NUMBERS
DAMD17-99-1-9121

6. AUTHOR(S)
Gregory S. Karczmar, Ph.D.

7. PERFORMING ORGANIZATION NAME(S) AND ADDRESS(ES)
The University of Chicago
Chicago, IL 60637

E-Mail: gskarczm@uchicago.edu

8. PERFORMING ORGANIZATION REPORT NUMBER

9. SPONSORING / MONITORING AGENCY NAME(S) AND ADDRESS(ES)
U.S. Army Medical Research and Materiel Command
Fort Detrick, Maryland 21702-5012

10. SPONSORING / MONITORING AGENCY REPORT NUMBER

11. SUPPLEMENTARY NOTES

12a. DISTRIBUTION / AVAILABILITY STATEMENT
Approved for Public Release; Distribution Unlimited

12b. DISTRIBUTION CODE

13. ABSTRACT (Maximum 200 Words)

The goal of this research is to use high spectral and spatial resolution (HiSS) MR imaging to improve images of human breast. Our work on the application of HiSS to improve anatomic and functional imaging was first described in a paper in Academic Radiology. Related work from this laboratory is presented in a number of other publications. Work from other laboratories shows that closely related methods also provide advantages for anatomic and functional MRI. Our funding from the Army has supported implementation of HiSS on clinical scanners and preliminary tests of the method in women with normal breasts and women with breast lesions. The results demonstrate that HiSS provides improved fat-suppression, contrast and edge delineation compared to conventional imaging. The funded work resulted in several publications listed in this report We are continuing to optimize this method and are applying for additional funding so that it can be tested in a larger group of women.

14. SUBJECT TERMS
Breast cancer, magnetic resonance imaging

15. NUMBER OF PAGES
38

16. PRICE CODE

17. SECURITY CLASSIFICATION OF REPORT Unclassified	**18. SECURITY CLASSIFICATION OF THIS PAGE** Unclassified	**19. SECURITY CLASSIFICATION OF ABSTRACT** Unclassified	**20. LIMITATION OF ABSTRACT** Unlimited

NSN 7540-01-280-5500

Standard Form 298 (Rev. 2-89)
Prescribed by ANSI Std. Z39-18
298-102

Table of Contents

(2) **INTRODUCTION:** Narrative that briefly (one paragraph) describes the subject, purpose, and scope of the research.

The goal of this research is to use high spectral and spatial resolution (HiSS) MR imaging to improve images of human breast. Our work on the application of HiSS to improve anatomic and functional imaging was first described in a paper in Academic Radiology [1]. Related work from this laboratory is presented in a number of other publications [2-9]. Work from other laboratories shows that closely related methods also provide advantages for anatomic [10] and functional [11-14] MRI.

This significant body of work provides support for the feasibility of ongoing experiments in this laboratory. Specifically, we expect to 1) improve separation of water and fat signals 2) increase image contrast 3) increase sensitivity to contrast agents and to local physiology – and as a result improve detection of suspicious lesions such as cancers and particularly delineation of tumor edges. We expect that this will increase the sensitivity and specificity of MR scans for breast cancer. To achieve these goals our original 'statement of work' was as follows:

A. Implementation of FSI methods on a clinical Scanner: Our clinical whole body scanners will be programmed to produce oscillating gradients during the decay of the proton FID so that a series of gradient echoes can be detected following excitation.

B. Processing FSI Data: Spectral information in FSI data sets will be analyzed to reduce the effects of resonance offset in MR images. Then the corrected FSI data will be used to synthesize images in which intensity is proportional to the peak intensity, linewidth, integral, and resonance frequency of resonances.

C. A phantom which contains large magnetic susceptibility gradients and both lipid and water compartments will be constructed to allow evaluation and optimization of FSI methods. Conventional spectroscopic images which use only phase encoding gradients to obtain spatial information will provide 'gold standard' images of the phantom.

D. Studies of patients: Women who are at increased risk for breast cancer and attend our 'high risk' clinic, and patients who are treated with neoadjuvant therapy for breast cancer will be recruited for MR studies:

1. Approximately 25 patients per year will be studied using fast spectroscopic imaging without contrast agents. **FSI** will be correlated quantitatively with conventional MRI and biopsy.

2. Approximately 25 patients per year will be given contrast. Time resolved FSI images of contrast uptake will be analyzed to measure rates of contrast uptake and accurately identify the boundaries of enhancing regions. T_1-weighted and T_2^*-weighted images of contrast agent uptake will be synthesized. **FSI** images will be correlated quantitatively with conventional MRI and biopsy

3. Quantitive analysis of FSI data and quantitative comparison with conventional images: We will extend previous work of Drs. Guilhuijs and Giger to provide quantitative analysis of **FSI** and conventional images. We will compare edge sharpness, texture, temporal and spatial gradients in contrast media uptake, signal-to-noise ratio, and contrast-to-noise ratio in FSI and conventional MR images.

E. MR data will be correlated with biopsy, conventional MR images, and mammography.

(3) **BODY:**

During the final year of funding we completed most of the specific aims of the proposal. We did the following work on each specific aim:

SOWA: This goal was completed during the first year of funding.

SOWB. We developed new approaches to acquiring and processing spectral/spatial data that improve image quality and reduce artifacts.

First, we developed a method for correcting spectroscopic data by accounting for errors in echo spacing. This reduced spectral ghost artifacts and improved the accuracy of the calculated spectra associated with each voxel.

Second: We applied parallel imaging methods to spectral/spatial imaging. Specifically we developed methods for coherently combining signals from different coil elements to increase signal-to-noise ratio of our data. We also began work towards use of parallel imaging to reduce HiSS data acquisition time.

Third: We developed software that corrects for residual macroscopic B_0 gradients. After this correction, the resonance frequency of the various components of the water resonance in each voxel more accurately reflects local susceptibility gradients that reflect local anatomy and physiology. This improves our spectral/spatial images – particularly images of the water resonance frequency. In addition, it facilitates Fourier Component imaging – this is a new concept that was developed in conjunction with this work (see below).

SOWD. Over the past year, we imaged women with suspicious lesions on mammography. Over the course of this grant we have scanned a total of about 70 patients. Approximately 40 of these were in the past year. Our more recent data supported our previous reports that fat-suppression, edge delineation, and image texture were improved in images derived from HiSS data compared to conventional images. HiSS data acquired pre- and post- contrast media injection showed features not evident in conventional images. A new paper describing the recent work was recently published in JMRI.

In conjunction with this work, we developed the concept of 'Fourier Component Imaging'. This is based on the hypothesis that the various components of the water resonance in each small image voxel reflect distinct anatomy and physiology. Therefore, images composed of the various Fourier Components of the water resonance show unique features – features that are not detected by conventional imaging. These features may be important clinically – for example, blood vessels associated with tumors may be detected. We have begun to test this concept by producing Fourier Component Images of the breast lesions we have imaged. A preliminary report of this work was accepted for oral presentation at the ISMRM this summer and a manuscript describing the work is currently being reviewed for publication in the Journal of Magnetic Resonance in Medicine.

The work is described in detail in the manuscripts that are included in the Appendix.

(4) KEY RESEARCH ACCOMPLISHMENTS: Bulleted list of **key** research accomplishments emanating from this research

- We have demonstrated how to implement high resolution spatial/spectral imaging on clinical scanners. Our work facilitates use of this method by other laboratories.
- We scanned a large number of women with suspicious breast lesions – approximately 70 over the course of this grant. The results demonstrated that HiSS imaging shows unique anatomy and physiology that is not seen in conventional images.
- We also performed quantitative analysis of HiSS and conventional image texture and edge delineation – demonstrating that HiSS increases these measures of image quality.

(5) REPORTABLE OUTCOMES:

Published papers during the last year:

1) HA Al-Hallaq, MA Zamora, BL Fish, HJ Halpern, JE Moulder, **GS Karczmar**. Using high spectral and spatial resolution bold MRI to choose the optimal oxygenating treatment for individual cancer patients. Adv Exp Med Biol **530**: 433-440, 2003

2) M Medved, W Du, MA Zamora, X Fan, OI Olopade, PM MacEneaney, G Newstead, **GS Karczmar**. The effect of varying spectral resolution on the quality of high spectral and spatial resolution magnetic resonance images of the breast. J Magn Reson Imaging **18**: 442-448, 2003.

3) W Du, YP Du, X Fan, MA Zamora, **GS Karczmar**. Reduction of spectral ghost artifacts in high-resolution echo-planar spectroscopic imaging of water and fat resonances. Magn. Reson Med **49**: 1113-1120, 2003.

Papers submitted:

M Medved, W. Du, X. Fan, M. Zamora, PM. Maceneaney, G. Newstead, and G.S. Karczmar. Images of the fourier components of the water resonance in breast", submitted to Magnetic Resonance in Medicine.

Presentations at International Meetings:

1) High Spatial and Spectral Resolution MR Imaging of Small Breast Lesions", M. Medved, G. Newstead, P. M. MacEneaney, M. A. Zamora, **G. S. Karczmar**, Oral Presentation at the Eleventh Scientific Meeting and Exhibition of ISMRM, Toronto, Canada, July 2003.

2) Images of the fourier components of the water resonance in breast", **G. S. Karczmar**, M. Medved, W. Du, X. Fan, M. Zamora, P. M. MacEneaney, Y.P. Du, F Kelcz and G Newstead, Oral Presentation at the Eleventh Scientific Meeting and Exhibition of ISMRM, Toronto, Canada, July 2003.

Degrees obtained for work supported by this award;

Al-Hallaq- Ph.D. awarded July, 2000

Weiliang Du, PhD. awarded December, 2003.

Sean Foxley, Ph.D. expected in 2007.

Funding awarded based on work supported by this award; Because of the success of the pilot work funded by this grant, applications for continued support from the NIH have been successful. An RO1 grant– supporting continued development of HiSS technology – has been funded by NIBIB - 1 R01 EB003108-01. An RO1 application to the NCI to support clinical evaluation of HiSS in women who are suspected to have ductal carcinoma in situ received a priority score in the 11.9 percentile. This is well within the proposed funding limit for the NCI and thus is highly likely to be funded.

Dissemination of HiSS Technology; Several institutions are interested in HiSS technology as a result of our work in this area. These laboratories include Dr. Alan Koretsky's laboratory at NIH, Dr. Robert Gillies laboratory at the University of Arizona at Tucson, Dr. Fred Kelcz's mammography service at the University of Wisconsin, Madison, and Dr. Nola Hylton's group at the University of California at San Francisco. We are helping these groups to implement technology developed as part of this award.

CONCLUSIONS: Our results to date demonstrate quantitatively that there are significant advantages associated with high spectral and spatial resolution imaging. These include

1. Detection of small lesions that are not visible with conventional imaging.
2. Often, small lesions can be detected even without contrast enhancement.
3. Greatly improved suppression of fat signals in breast
4. Improved delineation of edges, for example tumor boundaries
5. Greatly increased sensitivity to contrast agents.
6. Potential for sensitivity to subvoxelar environments – perhaps microscopic environments represented by the various components of inhomogeneously broadened water resonances.

We have received funding from the NIH that will allow us to continue work on important components of this research. Thus we believe that the funding from the Army has successfully advanced this technology so that this research can receive long-term support from the NIH. In addition this method has been incorporated into many clinical scans at the University of Chicago on a research basis. It is likely that it will soon be used clinically by our collaborators in the mammography section. We are also working to disseminate the HiSS technology that has been produced with DAMD funding. Several laboratories and mammography services have expressed interest in the technology and have asked for our help in implementing it.

REFERENCES:

1. Kovar, D. A.; Al-Hallaq, H. A.; Zamora, M. A.; River, J. N.; Karczmar, G. S. Fast spectroscopic imaging of water and fat resonances to improve the quality of MR images. Acad Radiol 5(4):269-275; 1998.

2. Kuperman, V.; River, J. N.; Karczmar, G. S. High Resolution Spectroscopic Images of Tumors. International Society for Magnetic Resonance in Medicine ; 1995.

3. Al-Hallaq, H. A.; Zamora, M.; Fish, B. L.; Farrell, A.; Moulder, J. E.; Karczmar, G. S. MRI measurements correctly predict the relative effect of tumor oxygenating agents on hypoxic fraction in rodent BA1112 tumors. Int J Radiat Oncol Biol Phys in press; 2000.

4. Al-Hallaq, H. A.; Karczmar, G. High resolution 1H spectroscopic imaging of the water and fat resonances in human breast. International Society for Magnetic Resonance in Medicine 2; 1997.

5. Al-Hallaq, H. A.; River, J. N.; Zamora, M.; Oikawa, H.; Karczmar, G. S. Correlation of magnetic resonance and oxygen microelectrode measurements of carbogen-induced changes in tumor oxygenation. Int J Radiat Oncol Biol Phys 41(1):151-159; 1998.

6. Karczmar, G. S.; Fan1, X.; Al-Hallaq1, H. A.; Zamora, M.; River, J. N.; Rinker-Schaeffer, C.; Zaucha, M.; Tarlo, K.; Kellar, K. Uptake of a Superparamagnetic Contrast Agent Imaged by MR with High Spectral and Spatial Resolution. Magnetic Resonance in Medicine 43:633-639; 2000.

7. Fan, X.; River, J. N.; Zamora, M.; Tarlo, K.; Kellar, K.; Rinker-Schaeffer, C.; Karczmar, G. S. Differentiation of Non-Metastatic and Metastatic Rodent Prostate Tumors with High Spectral and Spatial Resolution MRI. Magnetic Resonance in Medicine in press; 2001.

8. Karczmar, G.; X Fan1, H. A.-H.; River, J.; Tarlo, K.; Kellar, K.; Zamora, M.; Rinker-Schaeffer, C.; Lipton, M. J. Functional and Anatomic Imaging of Tumor Vasculature: High Resolution MR Spectroscopic Imaging Combined with a Superparamagnetic Contrast Agent. Academic Radiology in press; 2001.

9. Oikawa, H.; Al-Hallaq, H. A.; Lewis, M. Z.; River, J. N.; Kovar, D. A.; Karczmar, G. S. Spectroscopic imaging of the water resonance with short repetition time to study tumor response to hyperoxia. Magn Reson Med 38(1):27-32; 1997.

10. Sarkar, S.; Heberlein, K.; Metzger, G. J.; Zhang, X.; Hu, X. Applications of high-resolution echoplanar spectroscopic imaging for structural imaging. J Magn Reson Imaging 10(1):1-7; 1999.

11. Zhong, J.; Kennan, R.; Schaub, M.; Gore, J. C. Measurements of transient contrast enhancement by localized water NMR spectroscopy. J Magn Reson B 104(2):111-118; 1994.

12. Zhong, K.; Li, X.; Shachar-Hill, Y.; Picart, F.; Wishnia, A.; Springer, C. S. Magnetic susceptibility shift selected imaging (MESSI) and localized (1)H(2)O spectroscopy in living plant tissues. NMR Biomed 13(7):392-397; 2000.

13. Posse, S.; Wiese, S.; Gembris, D.; Mathiak, K.; Kessler, C.; Grosse-Ruyken, M. L.; Elghahwagi, B.; Richards, T.; Dager, S. R.; Kiselev, V. G. Enhancement of BOLD-contrast sensitivity by single-shot multi-echo functional MR imaging [In Process Citation]. Magn Reson Med 42(1):87-97; 1999.

14. Posse, S.; Dager, S. Using Functional Proton Spectroscopic Imaging. International Society for Magnetic Resonance in Medicine; 1995.

APPENDIX

M Medved, W Du, MA Zamora, X Fan, OI Olopade, PM MacEneaney, G Newstead, **GS Karczmar**. The effect of varying spectral resolution on the quality of high spectral and spatial resolution magnetic resonance images of the breast. J Magn Reson Imaging **18**: 442-448, 2003.

W Du, YP Du, X Fan, MA Zamora, **GS Karczmar**. Reduction of spectral ghost artifacts in high-resolution echo-planar spectroscopic imaging of water and fat resonances. Magn. Reson Med **49**: 1113-1120, 2003.

M. Medved, G. Newstead, X. Fan, W. Du, Y. Du, P.M. MacEneaney, R.M. Culp, F. Kelcz, O. Olopade, M.A.Zamora., G. Karczmar. Fourier Components of Inhomogeneously Broadened Water Resonances in Breast," submitted to Magnetic Resonance in Medicine.

APPENDIX 1

JOURNAL OF MAGNETIC RESONANCE IMAGING 18:442–448 (2003)

Original Research

The Effect of Varying Spectral Resolution on the Quality of High Spectral and Spatial Resolution Magnetic Resonance Images of the Breast

Milica Medved, PhD,[1]* Weiliang Du, MS,[1] Marta A. Zamora, BA,[1] Xiaobing Fan, PhD,[1] Olufunmilayo I. Olopade, MD,[2] Peter M. MacEneaney, MD,[1] Gillian Newstead, MD,[1] and Gregory S. Karczmar, PhD[1]

Purpose: To evaluate the effect of varying spectral resolution on image quality of high spectral and spatial resolution (HiSS) images.

Materials and Methods: Eight women with suspicious breast lesions and six healthy volunteers were scanned using echo-planar spectroscopic imaging (EPSI) at 1.5 Tesla with 0.75- to 1-mm in-plane resolution and 2.3- to 2.6-Hz spectral resolution. Time domain data were truncated to obtain proton spectra in each voxel with varying (2.6–83.3 Hz) resolution. Images with intensity proportional to water signal peak heights were synthesized. Changes in water signal line shape following contrast injection were analyzed.

Results: Fat suppression is optimized at $\sim$10-Hz spectral resolution and is significantly improved by removal of wings of the fat resonance. This was accomplished by subtracting a Lorentzian fit to the fat resonance from the proton spectrum. The water resonance is often inhomogeneously broadened, and very high spectral resolution is necessary to resolve individual components. High spectral resolution is required for optimal contrast in anatomic features with very high T_2* (e.g., within a lesion) and for detection of often subtle effects of contrast agents on water signal line shape.

Conclusion: Despite a trade-off between the spectral resolution and signal-to-noise ratio, it is beneficial to acquire data at the highest spectral resolution currently attainable at 1.5 Tesla.

Key Words: high spectral and spatial resolution spectroscopic imaging; echo-planar spectroscopic imaging; contrast agent effects; fat suppression; breast; cancer

J. Magn. Reson. Imaging 2003;18:442–448.

THE QUALITY OF MAGNETIC RESONANCE (MR) images of breast has been enhanced by a number of technical improvements, including improved fat saturation (1,2), Dixon-based methods (3–11) for improved fat and water separation, and dynamic contrast-enhanced MR imaging (MRI) (12–17). Despite these advances, the high sensitivity of MRI combined with limited specificity still leads to a large number of false positives (18–25). This is unacceptable if MRI is to be used in a large population of women, e.g., women who are at high risk for breast cancer.

High spectral and spatial resolution (HiSS) MRI increases the information content of MR data and, as a result, has the potential to increase sensitivity and specificity. HiSS data can be acquired rapidly using echo-planar spectroscopic imaging (EPSI) (26–28). The spatial resolution is similar to that of conventional clinical MRI or higher, and in addition, a high-resolution spectrum of the water and fat resonances is associated with each image voxel. This application of EPSI is different from the more common application to image metabolites at low resolution (29). The intent of HiSS is to produce improved anatomic and functional images of water- and fat-bearing tissue. Work in this laboratory demonstrated advantages of HiSS MRI of the breast (30). Other work suggests that spectral/spatial MRI in various forms, including multiple gradient echo imaging (31), is advantageous for functional and anatomic MRI (30–37). The advantages include improved fat suppression or fat/water separation, increased anatomic detail, and strong T_2* contrast with reduced artifacts due to intravoxel dephasing effects. In addition, HiSS increases sensitivity to effects of contrast agents. While conventional MRI detects only changes in T_1 and/or T_2*, HiSS can detect subtle changes in water resonance line shape following contrast media injection that may

---

[1] Department of Radiology, The University of Chicago, Chicago, Illinois.
[2] Section of Hematology and Oncology, The University of Chicago, Chicago, Illinois.

Contract grant sponsor: General Electric Medical Systems; Contract grant sponsor: Segal Foundation; Contract grant sponsor: Falk Medical Research Trust; Contract grant sponsor: Doris Duke Charitable Foundation; Contract grant sponsor: NCI; Contract grant numbers: RO1CA75476; RO1CA78803; Contract grant sponsor: Army Breast Cancer Research Program; Contract grant number: DAMD 17-99-1-9121.

Presented at the 10th Annual Meeting of ISMRM, Honolulu, 2002.

*Address reprint requests to: M.M., The University of Chicago, Department of Radiology, MC 2026, 5841 S. Maryland Ave., Chicago, IL 60637. E-mail: mmedved@uchicago.edu

Received November 4, 2002; Accepted May 27, 2003.
DOI 10.1002/jmri.10378

indicate subvoxelar regions of high vascular density (30,33,38). Studies of rodent prostate cancer suggested that HiSS MRI differentiates between metastatic and nonmetastatic cancers based on the texture, edges, and contrast media uptake characteristics in the primary tumor (38). However, high spectral resolution comes with a cost: it entails loss of signal-to-noise ratio (S/N) and increased image acquisition time. The purpose of the present work is to evaluate the effects of increasing spectral resolution on various anatomic and functional parameters in HiSS images of breast. This is accomplished by processing HiSS data sets at spectral resolutions ranging from 83.3–2.6 Hz.

MATERIALS AND METHODS

Patient Recruitment

Six women without evidence of breast abnormalities and eight women with mammographically suspicious breast lesions were scanned. This group included the six volunteers and five of six patients studied previously by Du et al (30), as well as three additional patients. The patients were recruited from the University Cancer Risk Clinic and the mammography service. The healthy volunteers were recruited from the clinic staff. All patients were studied under a protocol approved by the university Institutional Review Board after informed consent was obtained.

Image Acquisition

MR images were acquired on 1.5-Tesla GE SIGNA scanners equipped with ECHO SPEED™ GRADIENTS (GE Medical Systems, Waukesha, WI), with a maximum slew rate of 120 mT/m/second and maximum amplitude of 23 mT/m. The body coil was used for excitation and a phased array coil designed for breast imaging was used to detect signal. HiSS images were acquired using EPSI (26–28). The EPSI pulse sequence was composed of a slice-selective excitation pulse (4-mm slice thickness), a phase encoding gradient with 256 phase encoding steps, and a train of 128 gradient echoes with 256 sampled points per gradient echo. This produced images with in-plane resolution of 1 mm, and 128 bins of spectral resolution. The gradient echo train was sampled at a bandwidth of 62.5 kHz, so that the free ionization detector (FID) was sampled for 384 msec and the spacing between echoes was 3.0 msec. As a result, maximum spectral resolution was 2.6 Hz, or 0.041 ppm, and the spectral bandwidth was 333 Hz. The acquisition time per slice under these conditions was 128 seconds. (Three patients were imaged after a software upgrade on the scanner, with 384 sampled points per gradient echo, in-plane resolution of ~750 mm, spacing between echoes of 3.38 msec, FID sampling time of 432 msec, maximal spectral resolution of 2.31 Hz, and spectral bandwidth of 296 Hz.) The fat and water peaks were separated by more than 64 spectral bins, so that *N*/2 ghost peaks would not overlap fat or water signal. These ghost peaks are a consequence of the uneven sampling of the FID, analogous to the *N*/2 ghosting inherent to echo-planar imaging (EPI) sequences. Typically, only a single slice was imaged in each patient. Shimming was performed on the slice immediately before HiSS imaging. The patients were imaged both pre- and post-contrast agent injection (0.1 mM/kg of patient weight; Omniscan™, Nycomed Amersham; injected at rate of 2 mL/second), while the healthy volunteers did not receive contrast agent.

Image Processing

The raw EPSI data were processed into a form suitable for three-dimensional Fourier transformation, by excluding the file header and all data points that were not acquired as part of the echo train sequence. Even echoes were reversed, so that k-space was sampled in the same direction for odd and even echoes. A three-dimensional Fourier transform was applied to obtain a high-resolution proton spectrum in every voxel of the imaged slice. An algorithm was used on the resulting data to detect the fat and water peak frequencies in the following manner:

1. The highest peak in each voxel was identified, and a map of its frequency was generated.
2. The voxel of highest peak intensity was a priori identified by the software as either fat or water, and fat and water frequencies were determined for this voxel. Alternatively, one or more seed voxels were chosen in which the fat and/or water peaks were manually identified.
3. The voxel to be processed next, V_N, was selected as the highest peak height intensity voxel adjacent to the already processed voxels.
4. The frequency, f_{VN}, of the highest peak in V_N was compared to the expected fat frequency, f_{exp}, equal to the average of fat frequencies in neighboring, already processed voxels. Based on the separation of f_{VN} and f_{exp}, the highest peak in V_N was identified as either fat or water, and hence the fat frequency in V_N was determined.
5. The algorithm resumed at point 3, until all the voxels were processed, yielding a map of the fat frequency or, equivalently, the B_0 map.

In most cases, this algorithm did not require human intervention. It also effectively avoided errors due to Nyquist ghosting, inherent in EPI, and hence in EPSI. In our EPSI images, these show as spectral ghosts due to uneven sampling of the FID at high k_x values.

After the fat frequency map, and hence the water frequency map, was determined, water peak height images were constructed, as well as the analogous fat images. The high-resolution spectrum in each voxel was fitted using a Lorentzian approximation for the fat and water peaks and for any *N*/2 spectral ghosts. The Lorentzian fits for fat peaks and *N*/2 ghost peaks were then subtracted to allow accurate analysis of the water signal. This was particularly important for detection of small amounts of water in the presence of large fat signals. As the water signal was often inhomogenously broadened, the peak and integral water images were not obtained from the fit parameters. Rather, after subtraction of the fits for fat and *N*/2 ghosts, the maximum of the isolated water signal in each voxel was used to construct water peak height images.

This procedure was repeated to construct water peak height images at varying spectral resolutions. The spectral resolution was varied between 2.6 and 83.3 Hz by either using the full FID with all 128 echoes or truncating the FID at N = 64, 32, 16, 8, or 4 echoes and substituting the remaining echoes with zeros. This resulted in effective spectral resolutions of 2.6 (at full resolution), 5.2, 10.4, 20.8, 41.6, and 83.3 Hz. Truncation was preferred over exponential or other smoothing, as the purpose was to simulate faster data acquisition with a reduced number of echoes, rather than image processing methods.

Image Characterization

The quality of the water peak height images was assessed by quantifying fat suppression and image contrast. The region of interest selected for this analysis included the breast tissue and excluded signal from other sites, e.g., the chest wall. The effectiveness of fat/water separation was assessed by calculating a fat suppression ratio (FSR). We define FSR as the ratio of the average water peak height in the voxels containing predominantly water to that in the voxels containing predominantly fat (30). Due to the high spatial resolution of the images, all but a few voxels fall into one of these two categories. Since ideally only the water signal contributes to these images, signal in voxels that contain predominantly fat should be minimized, and signal in voxels that contain predominantly water should be maximized. Therefore, effective water/fat separation should increase FSR.

A texture parameter, S_r, which describes the nonuniformity of the measured intensity, S, was used to assess the contrast within the water image. S_r is defined as the increase in the surface area of the measured signal, (when intensity S is plotted against the xy position in the slice), relative to its projection, S_{xy}, onto the xy plane (30,38):

$$S_r = \frac{\sum \sqrt{1 + \left(\frac{\partial S}{\partial x}\right)^2 + \left(\frac{\partial S}{\partial y}\right)^2} - S_{xy}}{S_{xy}}. \qquad (1)$$

If image intensity in the region of interest is constant, S_r is 0. Highly variable image intensity results in a large S_r. No normalization of image intensities was performed, as we did not seek to compare images obtained in different exams to each other.

Contrast Agent Effects

To examine the effect of contrast agent, the postcontrast data were corrected for any in-plane global motion that might have occurred between the pre- and postcontrast acquisitions. Ten anatomical points of reference were selected, and their coordinates were recorded in pre- and post-contrast images. A least-squares fit was performed for six parameters of a linear transformation between these coordinates, correcting for translational and rotational motion and deformation. To obtain spectral amplitude in the motion-corrected image, bilinear interpolation was applied to the absolute value of spectral amplitude at the sampling points of new voxel coordinates. This procedure involved some smoothing between voxels, but dramatically improved the overlap of the pre- and postcontrast images. After the motion correction, the pre- and post-contrast water peaks were corrected for global B_0 shifts caused by the contrast agent (39).

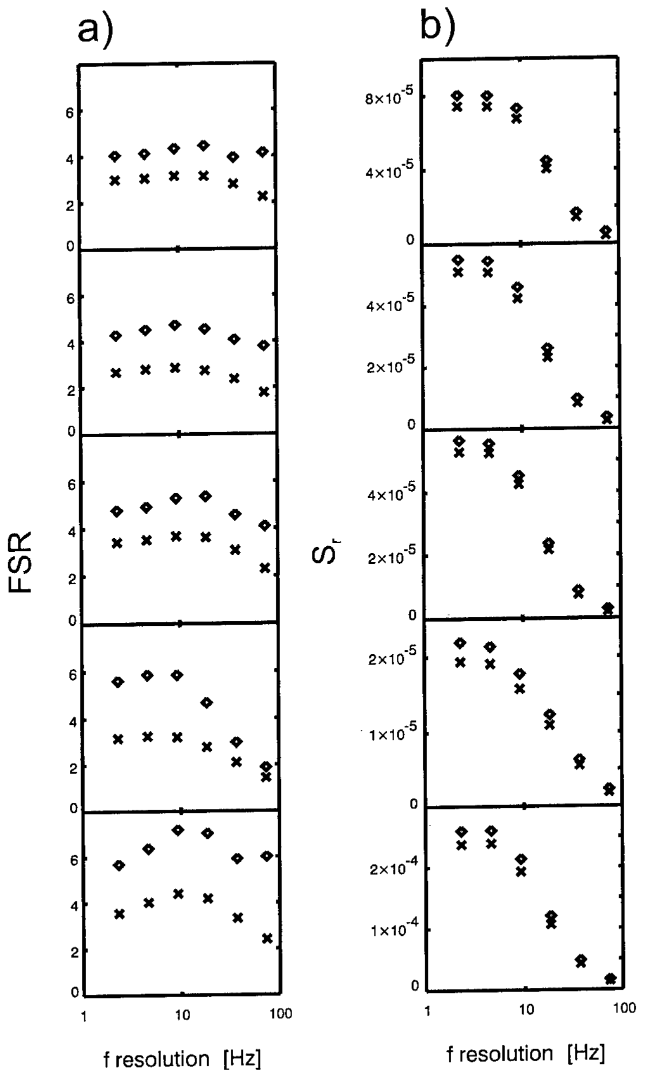

Figure 1. FSR, describing fat suppression in the image (**a**), and S_r, describing the contrast within the image (**b**), are calculated as a function of the frequency resolution. The frequency is shown on a logarithmic scale. For patients in the two bottom rows, the data were obtained in a slice that does not contain the lesion. Diamonds and crosses represent values obtained with and without subtracting the fat resonance, respectively.

RESULTS

Figure 1a shows the dependence of FSR in water peak height images on spectral resolution for three patients in which a breast lesion was imaged and for two in which a slice containing healthy tissue only was selected. The values shown in diamonds were determined

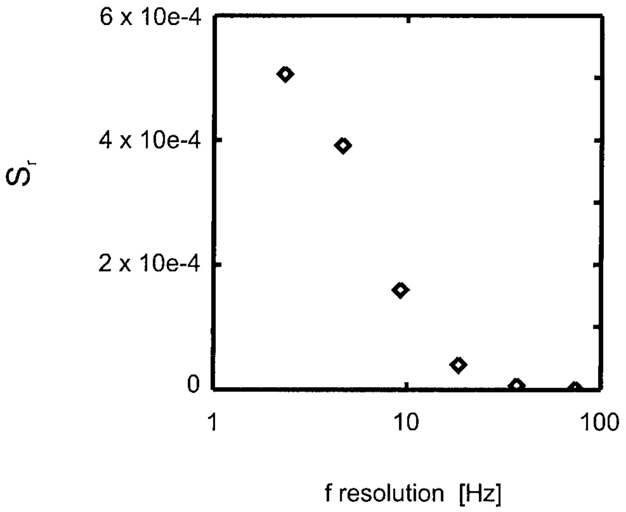

Figure 2. In certain regions within a lesion, S_r can show dramatic improvement at the highest spectral resolution. The data are from a patient not included in Fig. 1. S_r was calculated after subtracting the Lorentzian fit to the fat resonance.

by fitting the fat peak with a Lorentzian function and subtracting this Lorentzian fit from the proton spectrum to obtain an optimal value for water peak height in each voxel. The values shown in crosses were obtained from the peak height of the water resonance without subtracting the Lorentzian fit of the fat resonance. FSR is maximized at a spectral resolution of 10 to 20 Hz for all patients. Subtracting the Lorentzian approximation to the fat peak from the proton spectrum significantly improves the FSR.

In Figure 1b, the dependence of S_r on spectral resolution is plotted for the same five patients. Values obtained with (diamonds) and without (crosses) subtraction of the Lorentzian fit to the fat resonance are shown. Fitting the fat peak improves S_r slightly, but not as significantly as it does the FSR. In all cases, S_r increases dramatically with increased frequency resolution (to the left of the plot) and levels off at 5.2 Hz. However, the calculations of S_r performed on the whole breast may obscure improvements in the texture in smaller but critical regions with long T_2*, e.g., within the lesion. When S_r was calculated over smaller areas within the breast lesion, there were often improvements beyond 5.2 Hz. For one patient, the improvement in S_r between 5.2- and 2.6-Hz spectral resolution was as high as 29% (Fig. 2). For other patients, these improvements ranged between −12% and 12%, with an average improvement of 3%.

The advantages of peak fitting, evidenced in Figure 1, are greatest in the case where a small water resonance overlaps the wings of a very strong fat resonance. In Figure 3, this effect is even more significant as, due to the spectral wraparound, the water resonance appears at −0.5 ppm, very close to the fat peak (Fig. 3a). (The true frequency of the water resonance is set to 4.7 ppm.) The removal of the fat signal by peak fitting allows a much more accurate measurement of the amplitude of the small water signal (Fig. 3b). After subtraction of the Lorentzian fit, a residual fat peak, offset from the primary fat resonance, is evident in Figure 3b at ~0.5 ppm. However, it is small and offset from the water resonance and thus does not affect the water peak height.

Figure 4 shows the water peak height images for a patient with widespread intraductal carcinoma (upper row) and a patient with high-grade infiltrating ductal carcinoma (lower row), calculated at three different spectral resolutions: 2.6 Hz (N = 128), 10.4 Hz (N = 32), and 41.6 Hz (N = 8). At the highest spectral resolution (Fig. 4a), inhomogeneities within the lesions (arrows) are clearly visible, due to strong T_2* contrast in regions where T_2* is long. This contrast is reduced with reduced spectral resolution; this is particularly apparent in Figure 4c, where the lesions appear uniform.

Figure 5 shows spectra from four different voxels from one patient with infiltrating ductal carcinoma and one healthy volunteer, at full spectral resolution and at two lower spectral resolutions. With reduced spectral resolution (Fig. 5b), the S/N is significantly improved, as would be expected due to elimination of low S/N points at the end of the FID. However, details of the water resonance are obscured. The width of the water lines, obtained through fitting to a Lorentzian line shape, ranges between approximately 5 and 13 Hz, but at 41.6-Hz spectral resolution, the water resonance is significantly broadened and truncation artifacts are present. Even at 10.4-Hz spectral resolution, the small shoulders on the water resonance (indicated by arrows) are not resolved, as narrow spectral components are broadened. This may become an important consideration in contrast-enhanced MRI (see below). In pixel 2, the water resonance is clearly resolved only at the highest spectral resolution.

In Figure 6, the pre- (dashed line) and postcontrast (solid line) spectra from a single voxel are shown at two different resolutions: 2.6 Hz (Fig. 6a) and 10.4 Hz

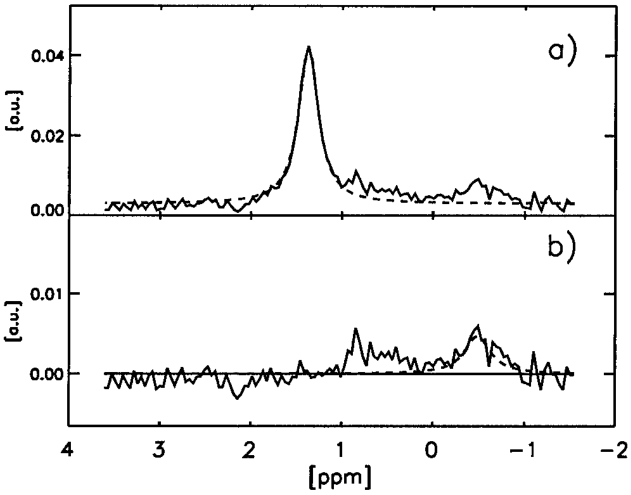

Figure 3. a: A proton spectrum for a representative voxel containing primarily fat (solid line) and the Lorentzian fit for the fat peak (dashed line) are shown. **b:** The same spectrum after the Lorentzian fit for the fat signal has been subtracted (solid line) shows the water peak much more clearly. A Lorentzian fit to the water peak is shown (dashed line). The vertical axis is shown in arbitrary units.

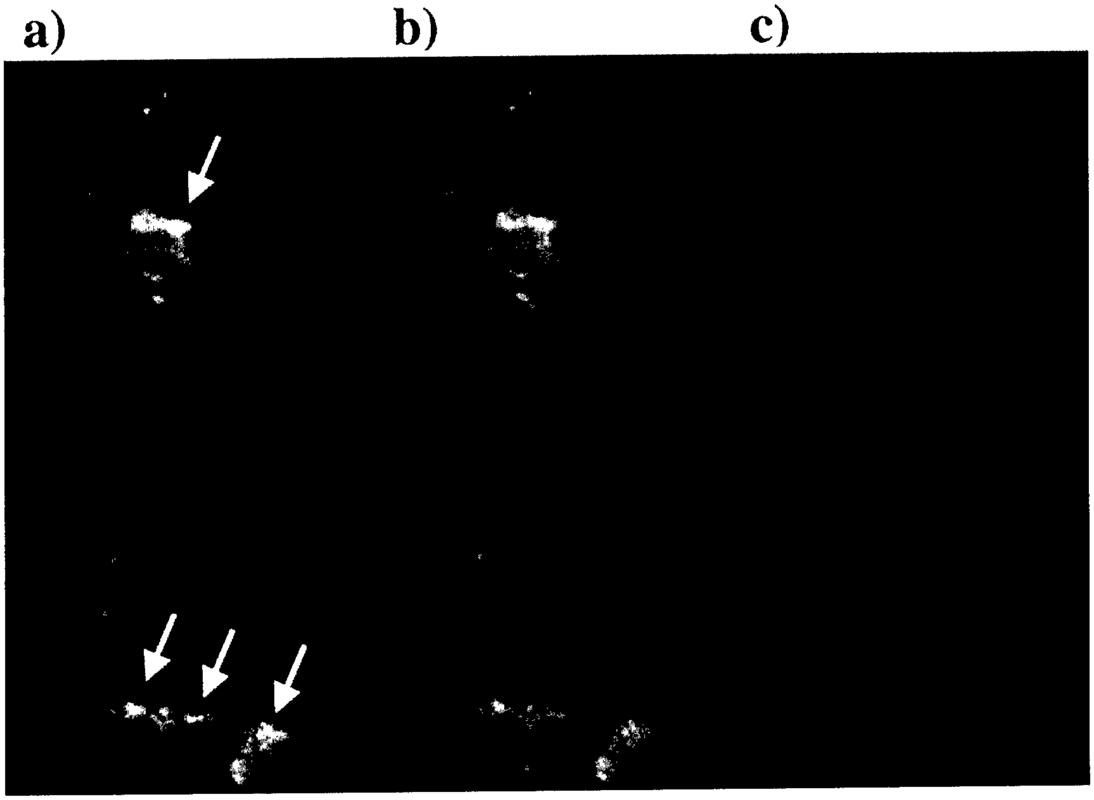

Figure 4. The water peak height images, calculated at varying spectral resolutions of 2.6 Hz (**a**), 10.4 Hz (**b**), and 41.6 Hz (**c**), are shown. The patients were diagnosed with widespread intraductal carcinoma (upper row) and with high-grade infiltrating ductal carcinoma (lower row). The arrows point to inhomogeneities in the lesions that are less prominent at lower spectral resolutions.

(Fig. 6b). At full spectral resolution, the inhomogenous broadening of the water line is clearly visible. A shoulder on the high-field side of the water resonance is much more clearly resolved after contrast injection (arrow). At the lower resolution, there is significant loss of detail in the water and fat signals, and the effect of the contrast agent is not accurately represented.

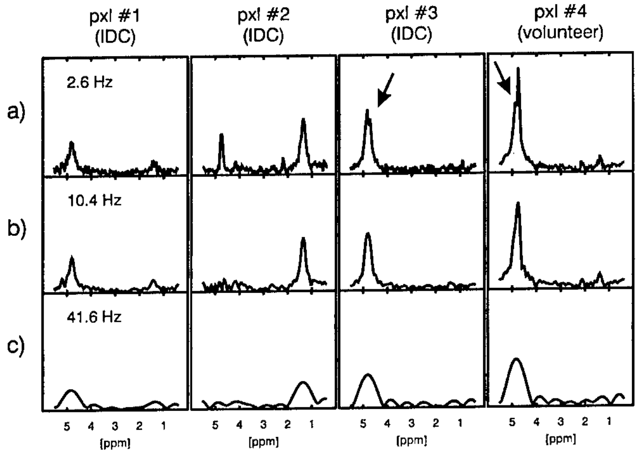

Figure 5. The proton spectra in four sample voxels from one patient with infiltrating ductal carcinoma (pixels 1–3) and one healthy volunteer (pixel 4) measured at varying spectral resolutions: 2.6 Hz (**a**), 10.4 Hz (**b**), and 41.6 Hz (**c**) are shown. The arrows point to shoulders in the water resonance that are not discernable in lower-spectral-resolution images. The water peak is placed at 4.7 ppm in all spectra. The vertical axis is shown in arbitrary units.

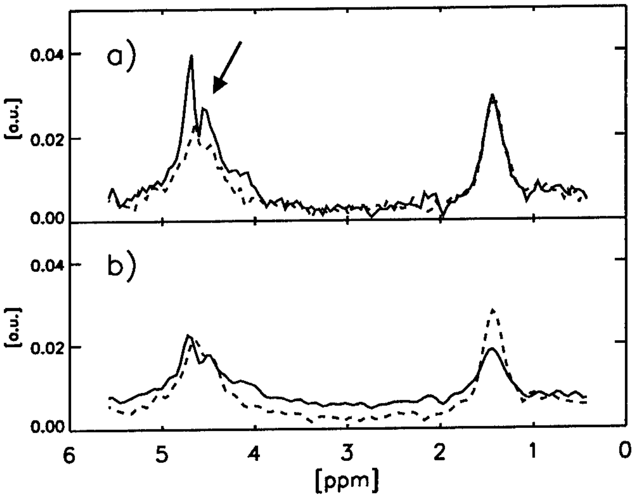

Figure 6. The pre- (dashed line) and post-contrast (solid line) spectra from a single voxel are shown at the maximum, 2.6 Hz (**a**), and a lower, 10.4 Hz (**b**), resolution. The arrow points to a shoulder on the water resonance, which is better resolved postcontrast at high resolution, but essentially unchanged at low resolution. The water peak is placed at 4.7 ppm. The vertical axis is shown in arbitrary units.

DISCUSSION

In human breast at 1.5 Tesla, high spectral resolution allows accurate measurement of narrow water lines and resolution of distinct components of inhomogeneously broadened water resonances (Fig. 5). The observed width of water and fat peaks ranges between approximately 5 and 13 Hz, and the resonances are broadened at resolutions lower than 10 Hz. At low resolutions, HiSS peak height images are roughly T1 weighted, while at the highest resolution, they combine T1 and strong T2* contrasts.

Spectral resolution of 5.2 Hz is generally acceptable for accessing T_2* variations contributing to increased contrast (Fig. 1), although in certain lesions, even better results can be obtained at a spectral resolution of 2.6 Hz (Fig. 2). This increased T_2* contrast, obscured at lower spectral resolutions (Fig. 4), reveals intralesion inhomogeneities important for lesion characterization, and is thus diagnostically valuable.

T_2* measurements have been performed previously by other researchers. For example, Kuperman and Alley (40) have used a faster three-dimensional sequence to obtain T_1- and T_2*-compensated images of breast. Kvistad et al (20) have used fast, lower-resolution T_2*-weighted images to measure perfusion in the breast. However, these sequences collect little spectral information and are not as heavily T_2* weighted as the data presented here. Our approach focuses instead on the detailed shape of the water line in small voxels, which can potentially be useful in producing new types of contrast at high spatial resolution, and for improving image quality by allowing separation of spectral and spatial information.

Spectrally inhomogeneous effects of contrast agents are resolvable at resolutions better than 10 Hz, allowing a novel approach to the use of contrast agents. Following contrast agent injection, it may be useful to measure changes in water signal line shape that are likely to be largely independent of the T_1 and T_2* changes measured by conventional MRI. In small voxels, each resolvable component of the water resonance may represent a different subvoxel population of water molecules in a discrete local magnetic environment. Thus, changes in resolvable components of the water signal following contrast media injection may reveal details of subvoxel physiology and anatomy that would be difficult or impossible to detect with conventional MRI. For example, shoulders that appear on the water resonance following contrast media injection may reflect the presence of subvoxelar regions with dense vasculature—an important marker for cancer. As these shoulders can be observed in both healthy and diseased tissue, an analysis of the contrast agent effect may be necessary for identification of cancerous tissue.

Maximum frequency resolution is not optimal for fat suppression. Rather, the FSR is maximized at approximately 10.6 Hz, with a slight decrease in FSR at higher spectral resolutions, presumably due to the reduced S/N. Therefore, for optimal water peak height images, under the present experimental conditions, it may be desirable to smooth the data to a resolution of 5–10 Hz, while optimal contrast in regions with long T_2* and detection of effects of contrast agents requires higher resolution.

Fitting the fat resonance to a Lorentzian function significantly improves fat suppression (Fig. 3a), allowing detection of small amounts of water in voxels where the fat signal is predominant. The improvement comes from removal of both the wings of the fat signal that may obscure a small water resonance and the baseline (noise) on which the water signal lies. In general, equivalent results are not achieved with fat saturation. Variations in B_0 across the breast cause significant problems for fat saturation. In addition, an inhomogenously broadened fat resonance would not be fully suppressed, even when the saturating pulse is at an optimal frequency, because of broad wings that sometimes include partially resolved shoulders. Fitting to a Lorentzian function accounts adequately for fat signal wings and the baseline, while in images obtained using fat saturation, the off-resonance fat signal often contributes to pixel intensity and may obscure small and/or diffuse cancers.

In a clinical setting, the current long acquisition time of HiSS images precludes scans of more than a few slices. Therefore, in its present form, this technique cannot be used as a screening (whole breast imaging) tool. Its greater value currently lies in diagnostics, where an evaluation of a previously discovered lesion or a suspicious region is needed and a limited section of the breast is imaged. This requires slice selection under the direct supervision of a radiologist who has localized the lesion based on previous mammographic, ultrasound, and/or MR exams. However, HiSS acquisition can be sped up by a factor of four or more by using parallel imaging and by scanning multiple lines of k-space in parallel (30). More efficient sampling of k-space and the FID will result in further time saving. Also, our data demonstrate that 5 Hz is an acceptable spectral resolution, which allows another factor of two in improvement in imaging time. All of these improvements will allow either a higher temporal resolution or coverage of a larger area with HiSS imaging.

Due to its current low time resolution, there are concerns about HiSS images suffering from artifacts, caused by changes in contrast agent concentration during acquisition, which would produce blurring along the phase encoding direction. We do not observe such artifacts in our HiSS images. This should not be surprising, as the time resolution of single-slice HiSS imaging (128 seconds) is comparable to that of sequences used for three-dimensional dynamic breast images, with two-dimensional phase encoding, in which data for each slice is generally acquired over 60–90 seconds. In addition, HiSS images presented here were not acquired during the first minute postcontrast, when the changes in the contrast agent concentration are most rapid.

In conclusion, we have demonstrated that at 1.5 T, improvements in fat suppression can be obtained at modest spectral resolution (~10 Hz). Higher spectral resolution yields improvements in anatomic detail in tumors, increased sensitivity to contrast agents, and strong T_2^* contrast. An analysis of the contrast agent effect on the water line shape may provide an important view of the tumor microenvironment. Combined with high spatial resolution, this new information can be pursued as a possible tool in earlier detection and more precise diagnosis of breast cancer.

REFERENCES

1. Soderstrom CE, Harms SE, Farrell Jr RS, Pruneda JM, Flamig DP. Detection with MR imaging of residual tumor in the breast soon after surgery. AJR Am J Roentgenol 1997;168:485–488.
2. Soderstrom CE, Harms SE, Copit DS, et al. Three-dimensional RODEO breast MR imaging of lesions containing ductal carcinoma in situ. Radiology 1996;201:427–432.
3. Chen Q, Schneider E, Aghazadeh B, Weinhous MS, Humm J, Ballon D. An automated iterative algorithm for water and fat decomposition in three-point Dixon magnetic resonance imaging. Med Phys 1999;26:2341–2347.
4. Wang Y, Li D, Haacke EM, Brown JJ. A three-point Dixon method for water and fat separation using 2D and 3D gradient-echo techniques. J Magn Reson Imaging 1998;8:703–710.
5. Daniel BL, Butts K, Glover GH, Cooper C, Herfkens RJ. Breast cancer: gadolinium-enhanced MR imaging with a 0.5-T open imager and three-point Dixon technique. Radiology 1998;207:183–190.
6. Szumowski J, Coshow W, Li F, Coombs B, Quinn SF. Double-echo three-point-Dixon method for fat suppression MRI. Magn Reson Med 1995;34:120–124.
7. Hardy PA, Hinks RS, Tkach JA. Separation of fat and water in fast spin-echo MR imaging with the three-point Dixon technique. J Magn Reson Imaging 1995;5:181–185.
8. Szumowski J, Coshow WR, Li F, Quinn SF. Phase unwrapping in the three-point Dixon method for fat suppression MR imaging. Radiology 1994;192:555–561.
9. Glover GH, Schneider E. Three-point Dixon technique for true water/fat decomposition with B0 inhomogeneity correction. Magn Reson Med 1991;18:371–383.
10. Glover GH. Multipoint Dixon technique for water and fat proton and susceptibility imaging. J Magn Reson Imaging 1991;1:521–530.
11. Dixon WT. Simple proton spectroscopic imaging. Radiology 1984; 153:189–194.
12. Nagashima T, Suzuki M, Yagata H, et al. Dynamic-enhanced MRI predicts metastatic potential of invasive ductal breast cancer. Breast Cancer 2002;9:226–230.
13. Hayes C, Padhani AR, Leach MO. Assessing changes in tumour vascular function using dynamic contrast-enhanced magnetic resonance imaging. NMR Biomed 2002;15:154–163.
14. Liu PF, Debatin JF, Caduff RF, Kacl G, Garzoli E, Krestin GP. Improved diagnostic accuracy in dynamic contrast enhanced MRI of the breast by combined quantitative and qualitative analysis. Br J Radiol 1998;71:501–509.
15. Mussurakis S, Gibbs P, Horsman A. Peripheral enhancement and spatial contrast uptake heterogeneity of primary breast tumours: quantitative assessment with dynamic MRI. J Comput Assist Tomogr 1998;22:35–46.
16. Kelcz F, Santyr GE, Cron GO, Mongin SJ. Application of a quantitative model to differentiate benign from malignant breast lesions detected by dynamic, gadolinium-enhanced MRI. J Magn Reson Imaging 1996;6:743–752.
17. Tofts PS, Berkowitz B, Schnall MD. Quantitative analysis of dynamic Gd-DTPA enhancement in breast tumors using a permeability model. Magn Reson Med 1995;33:564–568.
18. Kristoffersen Wiberg M, Aspelin P, Perbeck L, Boné B. Value of MR imaging in clinical evaluation of breast lesions. Acta Radiol 2002; 43:275–281.
19. Heywang-Köbrunner SH, Bick U, Bradley Jr WG, et al. International investigation of breast MRI: results of a multicentre study (11 sites) concerning diagnostic parameters for contrast-enhanced MRI based on 519 histopathologically correlated lesions. Eur Radiol 2001;11:531–546.
20. Kvistad KA, Rydland J, Vainio J, et al. Breast lesions: evaluation with dynamic contrast-enhanced T1-weighted MR imaging and with T2*-weighted first-pass perfusion MR imaging. Radiology 2000;216:545–553.
21. Kacl GM, Liu P, Debatin JF, Garzoli E, Caduff RF, Krestin GP. Detection of breast cancer with conventional mammography and contrast-enhanced MR imaging. Eur Radiol 1998;8:194–200.
22. Boné B, Péntek Z, Perbeck L, Veress B. Diagnostic accuracy of mammography and contrast-enhanced MR imaging in 238 histologically verified breast lesions. Acta Radiol 1997;38:489–496.
23. Boné B, Aspelin P, Bronge L, Isberg B, Perbeck L, Veress B. Sensitivity and specificity of MR mammography with histopathological correlation in 250 breasts. Acta Radiol 1996;37:208–213.
24. Kaiser WA. False-positive results in dynamic MR mammography. Causes, frequency, and methods to avoid. Magn Reson Imaging Clin N Am 1994;2:539–555.
25. Obdeijn IM, Kuijpers TJ, van Dijk P, Wiggers T, Oudkerk M. MR lesion detection in a breast cancer population. J Magn Reson Imaging 1996;6:849–854.
26. Mansfield P. Spatial mapping of the chemical shift in NMR. Magn Reson Med 1984;1:370–386.
27. Doyle M, Mansfield P. Chemical-shift imaging: a hybrid approach. Magn Reson Med 1987;5:255–261.
28. Nelson SJ, Vigneron DB, Star-Lack J, Kurhanewicz J. High spatial resolution and speed in MRSI. NMR Biomed 1997;10:411–422.
29. Pelletier D, Nelson SJ, Grenier D, Lu Y, Genain C, Goodkin DE. 3-D echo planar (1)HMRS imaging in MS: metabolite comparison from supratentorial vs. central brain. Magn Reson Imaging 2002;20: 599–606.
30. Du W, Du YP, Bick U, et al. Breast MR imaging with high spectral and spatial resolutions: preliminary experience. Radiology 2002; 224:577–585.
31. Yang QX, Demeure RJ, Dardzinski BJ, Arnold BW, Smith MB. Multiple echo frequency-domain image contrast: improved signal-to-noise ratio and T2 (T2*) weighting. Magn Reson Med 1999;41: 423–428.
32. Karczmar GS, Fan X, Al-Hallaq H, et al. Functional and anatomic imaging of tumor vasculature: high-resolution MR spectroscopic imaging combined with a superparamagnetic contrast agent. Acad Radiol 2002;9 (Suppl 1):S115–118.
33. Karczmar GS, Fan X, Al-Hallaq HA, et al. Uptake of a superparamagnetic contrast agent imaged by MR with high spectral and spatial resolution. Magn Reson Med 2000;43:633–639.
34. Posse S, Wiese S, Gembris D, et al. Enhancement of BOLD-contrast sensitivity by single-shot multi-echo functional MR imaging. Magn Reson Med 1999;42:87–97.
35. Sarkar S, Heberlein K, Metzger GJ, Zhang X, Hu X. Applications of high-resolution echoplanar spectroscopic imaging for structural imaging. J Magn Reson Imaging 1999;10:1–7.
36. Kovar DA, Al-Hallaq HA, Zamora MA, River JN, Karczmar GS. Fast spectroscopic imaging of water and fat resonances to improve the quality of MR images. Acad Radiol 1998;5:269–275.
37. Oikawa H, Al-Hallaq HA, Lewis MZ, River JN, Kovar DA, Karczmar GS. Spectroscopic imaging of the water resonance with short repetition time to study tumor response to hyperoxia. Magn Reson Med 1997;38:27–32.
38. Fan X, River JN, Zamora M, et al. Differentiation of nonmetastatic and metastatic rodent prostate tumors with high spectral and spatial resolution MRI. Magn Reson Med 2001;45:1046–1055.
39. Al-Hallaq HA, Fan X, Zamora M, River JN, Moulder JE, Karczmar GS. Spectrally inhomogeneous BOLD contrast changes detected in rodent tumors with high spectral and spatial resolution MRI. NMR Biomed 2002;15:28–36.
40. Kuperman VY, Alley MT. Differentiation between the effects of T1 and T2* shortening in contrast-enhanced MRI of the breast. J Magn Reson Imaging 1999;9:172–176.

APPENDIX 2

Magnetic Resonance in Medicine 49:1113–1120 (2003)

Reduction of Spectral Ghost Artifacts in High-Resolution Echo-Planar Spectroscopic Imaging of Water and Fat Resonances

Weiliang Du,[1] Yiping P. Du,[2] Xiaobing Fan,[1] Marta A. Zamora,[1] and Gregory S. Karczmar[1]*

Echo-planar spectroscopic imaging (EPSI) can be used for fast spectroscopic imaging of water and fat resonances at high resolution to improve structural and functional imaging. Because of the use of oscillating gradients during the free induction decay (FID), spectra obtained with EPSI are often degraded by Nyquist ghost artifacts arising from the inconsistency between the odd and even echoes. The presence of the spectral ghost lines causes errors in the evaluation of the true spectral lines, and this degrades images derived from high-resolution EPSI data. A technique is described for reducing the spectral ghost artifacts in EPSI of water and fat resonances, using echo shift and zero-order phase corrections. These corrections are applied during the data postprocessing. This technique is demonstrated with EPSI data acquired from human brains and breasts at 1.5 Tesla and from a water phantom at 4.7 Tesla. Experimental results indicate that the present approach significantly reduces the intensities of spectral ghosts. This technique is most useful in conjunction with high-resolution EPSI of water and fat resonances, but is less applicable to EPSI of metabolites due to the complexity of the spectra. Magn Reson Med 49:1113–1120, 2003. © 2003 Wiley-Liss, Inc.

Key words: artifact; odd and even echoes; echo-planar spectroscopic imaging; spectral ghost artifacts; high spectral and spatial resolution imaging

The desire to shorten imaging time has stimulated the use of fast alternating gradients in many MRI methods. Echo-planar spectroscopic imaging (EPSI) uses an alternating readout gradient for simultaneous encoding of the chemical shift dimension and one spatial dimension, and phase-encoding gradients for the other spatial dimensions. This strategy was first proposed by Mansfield (1) and has been successfully advanced by Posse et al. (2,3) and other workers for metabolite imaging (4–9), water and fat structural imaging (10–14), and functional imaging (3,15,16).

Compared to conventional phase-encoded spectroscopic imaging (SI), EPSI has the advantage of significantly reduced scan time; however, it places strong demands on the MR system, especially the gradient hardware. Inconsistency (i.e., discontinuity in magnitude and phase) between the odd and even echoes often arises because of the use of the echo-planar gradients. This effect is well known in echo-planar imaging (EPI). In EPI, the inconsistency causes Nyquist image ghosts in the phase-encoding dimension, since the odd and even echoes represent interlaced phase-encoded lines in *k*-space (17). Because the odd and even echoes encode the spectral dimension in EPSI, the signal inconsistency causes Nyquist ghosts in resulting spectra. The spectral ghosts are detrimental in two ways. First, the ghost peak of one true peak may appear on top of or near a second true peak, impeding accurate quantification of the latter peak and altering the lineshape. Second, the intensity of the true peak is reduced because of the "energy leakage" from the true peak to the ghost peak. The spectral ghosts are especially problematic when EPSI is used for high spectral and spatial (HISS) imaging (10,11,16) where the goal is to obtain detailed water and fat spectra for anatomic and functional imaging.

A number of techniques have been proposed for the reduction of spectral ghost artifacts. One widely used and effective method is to separate the odd and even echoes in data processing (2,13,15). Unfortunately, this sacrifices half of the spectral bandwidth, which is already small in high spatial resolution EPSI. Alternatively, the odd and even echoes are combined for processing using the interlaced Fourier transform method (6) or the Fourier shift method (18). These techniques address the issue of nonuniform temporal sampling arising from the evolution of the free induction decay (FID) during each gradient echo. With these approaches, it is implicitly assumed that data are precisely sampled along a theoretically determined trajectory in *k-t*-space. In other words, the odd and even echoes are properly aligned and no corrections are made to the data at the center of *k*-space. In practice, this assumption is often invalid. Echo misalignments and distortions often lead to Nyquist ghosts in images obtained with EPI (17), and should be accounted for. Corrections for echo misalignment have been developed for EPSI by measuring the *k-t* trajectory and interpolating data at the desired locations (6,13). The main drawback of this method is the complicated procedure required for *k-t* trajectory measurement.

In this article, we present a new method to reduce the spectral ghost artifacts in EPSI by correcting the echo misalignment and phase discontinuities between the odd and even echoes. This approach is conceptually an extension of the echo shifting and phase correcting method that has been effective in removing inconsistency between the odd and even echoes for EPI data (17). The echo misalign-

---

[1] Department of Radiology, University of Chicago, Chicago, Illinois.

[2] Department of Psychiatry and Radiology, University of Colorado Health Sciences Center, Denver, Colorado.

Grant sponsor: NCI; Grant numbers: RO1CA75476; RO1CA78803; Grant sponsor: Army Breast Cancer Research Program; Grant number: DAMD 17-99-1-9121; Grant sponsor: General Electric.

*Correspondence to: Gregory S. Karczmar, Ph.D., Department of Radiology, MC 2026, University of Chicago, 5841 S. Maryland Ave., Chicago, IL 60637. E-mail: gskarczm@midway.uchicago.edu

Received 8 October 2002; revised 13 January 2003; accepted 6 February 2003.

DOI 10.1002/mrm.10485

ment is corrected by shifting the "centers of mass" (CM) of the odd and even echoes, and a zero-order phase correction is then applied to the odd echoes to minimize the spectral ghost intensity. This method takes advantage of the high SNR signals at the k-space center to measure inconsistencies in position and phase between the odd and even echoes. All corrections are made during data postprocessing, i.e., without the need for additional reference scans.

This technique has been applied to high spatial resolution EPSI data obtained from human brains and breasts at 1.5 Tesla, and from a water phantom at 4.7 Tesla. The MR images were acquired using an EPSI sequence without water or fat suppression. Water and fat spectra obtained with the present method and the conventional FFT method were compared to demonstrate the effectiveness of the new method.

MATERIALS AND METHODS

Data Acquisition

EPSI Pulse Sequence

The EPSI pulse sequence we implemented was a gradient-recalled multiecho sequence with 64 or 128 gradient echoes excited along the x dimension using trapezoidal readout gradients. The second spatial dimension (y) was provided by phase-encoding gradients between excitation and detection.

To provide sufficient spectral bandwidth, we collected the EPSI data in multiple (N_{int}) acquisitions. In each acquisition (or interleaf) the temporal offset of the echo train from the excitation pulse was incremented by Δt. This effectively reduced the time interval between adjacent gradient echoes (i.e., echo spacing, or $T_{esp} = N_{\text{int}}\Delta t$), and thus increased the spectral bandwidth by a factor of N_{int}.

Phantom Studies

Phantom experiments were performed on a 4.7 Tesla magnet (Omega; GE/Bruker, Fremont, CA). The phantom was a bottle of copper sulfate solution with an inner diameter of 24 mm. EPSI scans were performed through a 1-mm-thick axial slice with an in-plane resolution of 0.38×0.38 mm^2 and a field of view (FOV) of 48 mm. The readout gradient consisted of 64 alternating lobes, each of which had two linear ramps (0.5 ms each) and a plateau (3.2 ms). Data were sampled only during the plateau phase of the gradient. The echo train lasted for 270 ms, yielding spectral resolution of 3.7 Hz. Interleaved EPSI datasets ($N_{\text{int}} = 2$) were acquired with an echo train offset of 2.1 ms so that the combination of the two interleaves resulted in a spectral bandwidth of 473 Hz. Each EPSI interleaf was acquired in 128 s (TR = 1 s).

Human Studies

Healthy volunteers were imaged on a 1.5 Tesla MR scanner (Signa; GE Medical Systems, Milwaukee, WI), following a protocol approved by the University of Chicago Institutional Review Board. EPSI images were obtained in an axial slice through the brains ($N = 8$) or in a sagittal slice through the breasts ($N = 2$, female). Imaging parameters were: TR = 500 ms, sampling bandwidth = ±62.5 kHz, slice thickness = 4 mm, FOV = 24 cm, spectral bandwidth = 333 Hz, matrix size = 256 (x) × 256 (y) 128 (f), and $N_{\text{int}} = 1$. The EPSI scan was acquired in 128 s.

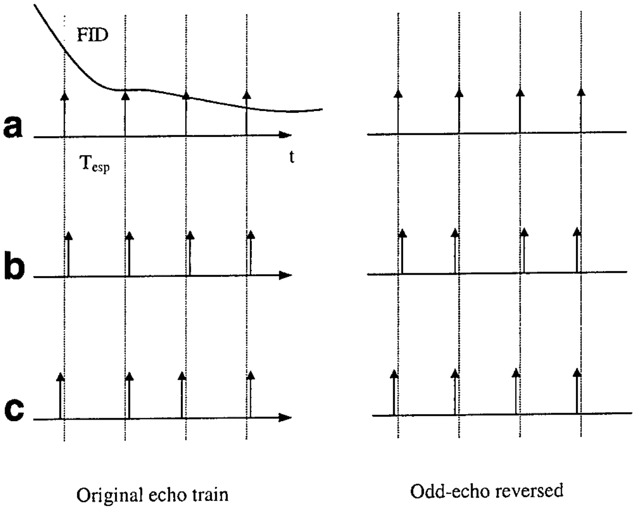

FIG. 1. Misalignment of the gradient echoes before (left) and after (right) the reversal of the odd echoes. The short arrows indicate the position of $k_x = 0$ point in each echo. **a:** Ideal alignments. **b:** A temporal shift of the entire echo train. **c:** Uneven spacing between adjacent echoes.

Postprocessing

Echo Misalignment

In an ideal EPSI experiment, the center of k-space (i.e., the $k_x = 0$ point) is traversed repeatedly with a constant time interval (Fig. 1a). Because of the opposite directions of the trajectories along k_x caused by the alternating readout gradients, the odd (or even) echoes must be reversed during data processing; however, the alignment of the $k_x = 0$ points does not change in the ideal situation. Two types of echo misalignments occur in practice due to various scanner- or sample-related imperfections. In the first type (Fig. 1b), the echo train is temporally shifted relative to the start of data acquisition, due to system timing errors, imperfection of gradient hardware (6,13), and uncompensated eddy currents (19,20). The reversal of the odd echoes translates this temporal shift in the echo train into a relative misplacement along k_x between the odd and even echoes. This misplacement generates spectral ghost artifacts when the echoes are used to produce spectra. In the second type of echo misalignment (Fig. 1c), the odd and even echoes are unevenly spaced within the echo train. This misalignment may be due to background gradients resulting from improper shimming, local susceptibility inhomogeneity, and eddy currents (21), or to an inaccurate dephasing gradient applied along k_x before the alternating readout gradients. As a result, the FID signals are not uniformly sampled at all k-space positions, including the $k_x = 0$ point, which introduces apparent magnitude and phase discontinuities between the odd and even samples, and thus generates spectral ghosts.

Echo Shift Correction

Previous EPSI studies either assumed an ideal echo misalignment (18) (i.e., no corrections are made to signals at *k*-space center) or corrected the first type of echo misalignment described above based on a predetermined *k*-space trajectory (6,13). In this study we corrected for the first type of echo misalignment by shifting the positions of the odd and even echoes using the information derived from the EPSI data itself. The raw data in the form of echo trains were grouped into a 3D signal matrix, $S(k_x, k_y, n)$, where n indexed the echoes (0, 1, 2, . . .) in the echo train and the odd echoes (n = 1, 3, . . .) were reversed. Then the *k*-space center ($k_x = 0$, $k_y = 0$) was approximated as the CM of the *k*-space signals for each echo, using the following formula:

$$CM_{kx}(n) = \frac{\sum\limits_{k_x,k_y} k_x \cdot |S(k_x, k_y, n)|}{\sum\limits_{k_x,k_y} |S(k_x, k_y, n)|}$$

$$CM_{ky}(n) = \frac{\sum\limits_{k_x,k_y} k_y \cdot |S(k_x, k_y, n)|}{\sum\limits_{k_x,k_y} |S(k_x, k_y, n)|}. \qquad [1]$$

The differences between the CMs of the first five even echoes and the CMs of the immediately adjacent five odd echoes (after reversal of odd echoes) were calculated and averaged. These echoes were used because of their relatively high signal-to-noise ratio (SNR). Half of the averaged difference was used to shift the original echo train (i.e., before the odd echoes were reversed). Shifts that were smaller than one data point were performed using the Fourier shift theorem (i.e., data were Fourier transformed, a linear phase term was added, and then data were inversely Fourier transformed). The shifted echo train data were then regrouped into the matrix $S(k_x, k_y, n)$ for further processing.

Phase Correction

Echo misalignment of the second type described above led to nonuniform sampling of FID signals at all *k*-space points. Instead of assuming a uniform sampling at k_x = 0 and correcting the phases of the signals at other *k*-space points (6,18), we used a constant phase factor to correct for the phases of the odd echo signals at all *k*-space points. The phase factor was derived from the EPSI data itself, as follows:

1. For each echo n, the middle point (presumably, $k_x = k_y = 0$) of the signal matrix S was extracted. A function, named $\mathrm{FID}_{k00}(n)$, was formed with the extracted samples and was Fourier transformed. In the EPSI data from water phantom and human brains, two peaks arose in the resulting spectrum that were exactly half of the spectral bandwidth apart. The peak with larger magnitude was identified as the "true" water peak, while the other peak was regarded as the "ghost" peak. In the case of breast EPSI, the resulting spectrum often consisted of a relatively strong fat peak, a relatively strong water peak ~216 Hz away (~3.4 ppm) from the fat peak, and two smaller peaks located half of the spectral bandwidth away from the fat peak and the water peak, respectively. We picked the peak with the largest magnitude (either the fat peak or the water peak) as the "true" peak, and the peak at half of spectral bandwidth away from this peak as the "ghost" peak.
2. The magnitudes of the true peak and the ghost peak were quantified as a summation of spectral intensities over a narrow neighborhood (e.g., 3–5 bins wide). Baseline was removed prior to the spectral summation, by subtracting a smoothed spectrum (boxcar length of ~15 bins) from the original spectrum. The ratio of the magnitude of the ghost peak to the magnitude of the true peak is herein referred to as the "ghost-to-true ratio" (GTR).
3. A phase angle ϕ was chosen from the range $(-\pi, \pi)$. A phase term $e^{-j2\pi\phi}$ was multiplied to the signals of the odd echoes at all *k*-space points. Steps 1 and 2 were repeated and the GTR was reevaluated.
4. The amount of phase correction was found using a Golden Section algorithm such that GTR was minimized.

Interleaved Acquisition

The correction methods described above were also extended to correct for the global phase changes in interleaved EPSI data. Each interleaf was treated separately with the echo shift and phase corrections described above. Then the interleaves were combined and a zero-order phase correction was applied to each interleaf (i.e., all echoes in that interleaf) except the first interleaf, in order to force the phase of every interleaf to be consistent with the first one. This zero-order phase correction was similar to the phase correction described above, except that the minimization problem in step (4) became multidimensional ($N_{\mathrm{int}}-1$). An IDL (Research Systems, Boulder, CO) routine employing the Powell's minimization algorithm was used in this task.

Method Evaluation

The EPSI spectrum in each pixel was obtained with a 3DFT following the echo shift and phase corrections. Images were formed with intensities proportional to the magnitude of the true peak, the magnitude of the ghost peak, and their ratio (GTR) using uncorrected and corrected spectra in each pixel. These variables were also reported quantitatively. To take the variation of these variables across the image into account, we pooled the measurements from all pixels with maximum spectral intensity 10 times above the noise level. Since these variables (e.g., GTR) did not necessarily follow a Gaussian distribution, we reported the median of pooled data along with the 20% and 80% quantiles as an estimate of the range of the measured variables.

RESULTS

Phantom

The CM calculated from the phantom EPSI data exhibits oscillatory displacements between the odd and even echoes in the readout (k_x) direction (Fig. 2a). Oscillation in CM is not seen in the phase-encoding (k_y) direction in the same EPSI data. Conventional phase-encoded SI (i.e., no

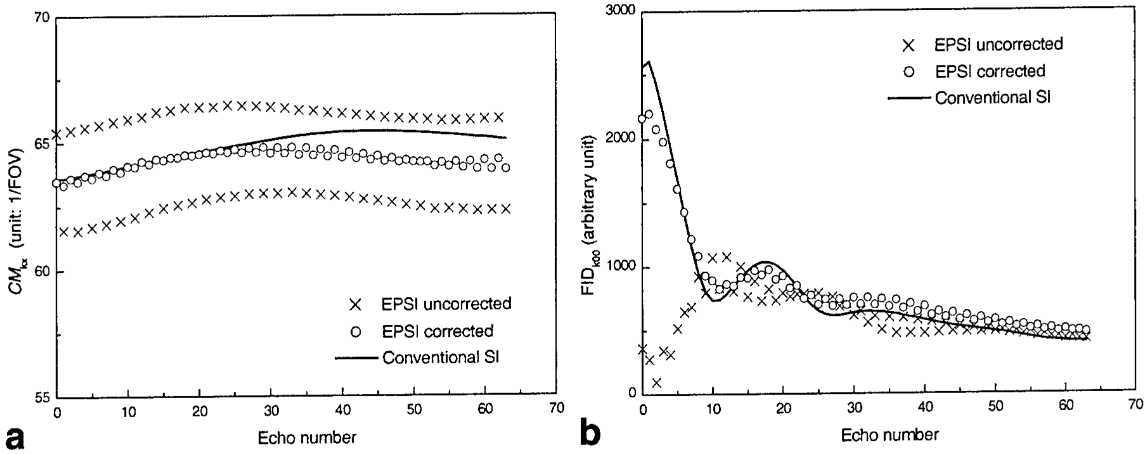

FIG. 2. Echo shift correction in EPSI data obtained from a water phantom. **a:** CM_{kx} (defined in Methods) as a function of the index of the echoes in uncorrected EPSI (cross), EPSI with echo shift correction (circle), and conventional phase-encoded SI (solid line). **b:** The magnitude of FID_{koo} from uncorrected EPSI, corrected EPSI, and conventional SI.

readout gradients) of the same slice under the same shim conditions shows similar overall trends of CM shifts, but no oscillatory pattern in either the k_x or the k_y dimensions. This excludes the possibility that the relative echo shift in the readout direction (k_x) is due to the nature of the imaged object, or to off-resonance effects such as background gradients. The echo misalignment is evidently related to the alternating readout gradient and relevant data acquisition. A temporal offset (66 μs, or 2.65 data points) was used for the echo shift correction. As a result, the CM of the corrected EPSI data shows a reduced amplitude of oscillation and approaches the CM obtained with the conventional SI data (Fig. 2a). Also, the shape of the corrected FID_{koo} shows much better agreement with the FID_{koo} measured with the conventional SI (Fig. 2b).

For the first interleaf of the phantom EPSI data, the GTR was minimized with a phase correction of $\phi = 40.7°$. For the second interleaf, the GTR was minimized with $\phi = 41.8°$. To combine the two interleaves, a phase correction of 0° was found to be necessary to correct for all echoes from the second interleaf. Nonzero phase corrections were made to the interleaves in other EPSI scans (data not shown here).

The EPSI data were also reconstructed without echo shift and phase corrections. A true water peak and three ghost peaks were found in the uncorrected spectra from most pixels. Figure 3 shows images synthesized from the peak height of the true water peak and the peak heights of the ghost peaks. Bright and dark streak patterns are evident in all uncorrected images. Where the signal intensity is strong in the ghost peaks (areas of hyperintensity in b, c, and d), the signal intensity is weak in the true water peak (areas of hypointensity in a). These artifacts are removed in the corrected peak height image (e). The intensities of the ghost peaks drop substantially (b vs. f, c vs. g, d vs. h) as the intensities of the true peaks increase (a vs. e), especially in pixels that originally had strong spectral ghosts. Table 1 summarizes the reduction of spectral ghosts in one- and two-interleaf EPSI datasets obtained with the water phantom.

Human Brain and Breast

Figure 4 demonstrates the effectiveness of the correction method on the EPSI data obtained from human brain. The ghost peaks are reduced to noise level in all pixels. The magnitudes of the true water peak increase nonuniformly across the image after the corrections. The increase is relatively large at locations where the spectral ghost is strong (near the edges of the brain). Table 2 shows the

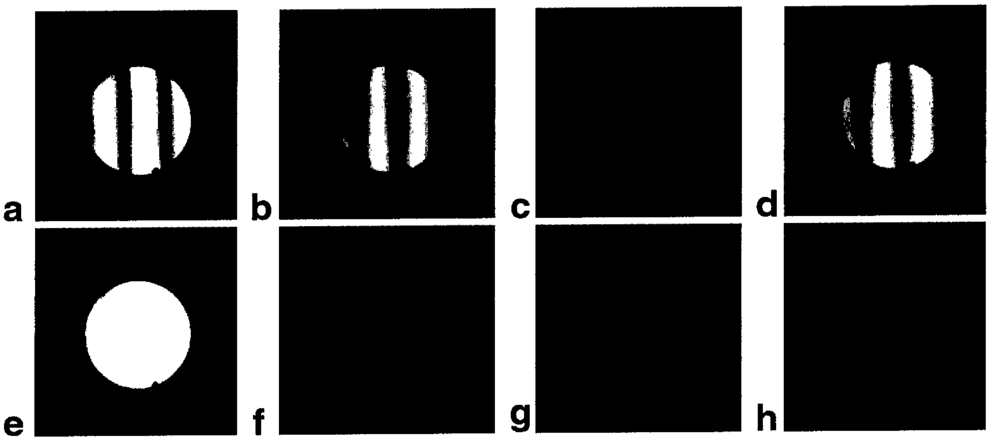

FIG. 3. Images synthesized from interleaved ($N_{int} = 2$) EPSI data without (upper panels) and with (lower panels) echo shift and phase corrections. From left to right, image intensity is proportional to the magnitude of the spectral peak at f_0 (**a** and **e**), $f_0 + bw/4$ (**b** and **f**), $f_0 + bw/2$ (**c** and **g**), and $f_0 + bw \cdot 3/4$ (**d** and **h**), where bw is the spectral bandwidth, f_0 is the frequency of the true water peak. The alternating readout gradient was applied in the horizontal direction.

Table 1
Reduction of the Spectral Ghost Peaks With the Echo Shift Correction and/or Phase Correction in EPSI Scans of a Water Phantom at 4.7 T*

	One-interleaf EPSI				Two-interleaf EPSI	
	Uncorrected	Echo shift correction only	Phase correction only	Echo shift and phase correction	Uncorrected	Echo shift and phase correction
Magnitude of true peak	3.40 (1.22, 5.01)	4.93 (4.76, 5.31)	3.46 (1.19, 5.13)	5.26 (5.09, 5.64)	4.31 (1.66, 6.22)	6.36 (6.17, 6.75)
Magnitude of ghost peak	3.65 (1.30, 5.15)	1.38 (1.11, 1.61)	3.63 (1.32, 5.08)	0.15 (0.06, 0.24)	2.14 (0.94, 2.84)	0.22 (0.17, 0.31)
Ghost-to-true ratio[a]	1.05 (0.25, 4.31)	0.28 (0.23, 0.32)	1.03 (0.25, 4.07)	0.027 (0.011, 0.046)	0.49 (0.15, 1.76)	0.035 (0.027, 0.048)

*The data presented are 50% (i.e., median) and 20%, 80% quantiles (in parenthesis) of the measurements obtained over an ROI covering most area of the phantom.

[a] Ghost-to-true ratio is defined as the ratio of magnitude of the ghost peak to the magnitude of the true water peak (also see Materials and Methods).

quantitative results of spectral ghost reduction. The EPSI datasets are corrected with an echo shift of approximately 0–7 μs and a zero-order phase of approximately −4° to 2°. The median of GTR before correction ranges from 2.4% (volunteer 5) to 27% (volunteer 2), with an average of approximately 12%. After the corrections, the median of GTR decreases to between 2% and 5%, with an average of 3.5%. The original GTRs are large in volunteers 2 and 4;

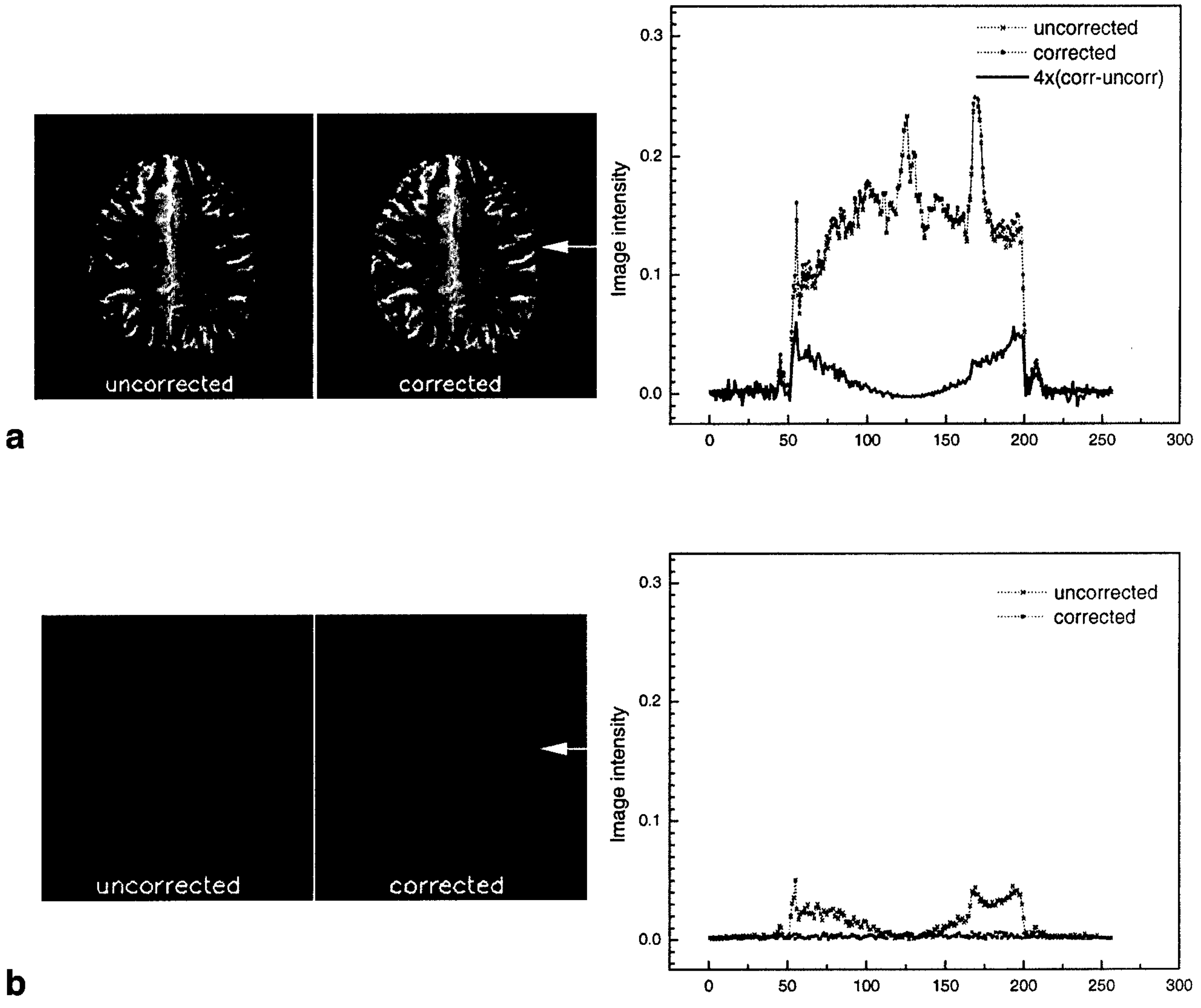

FIG. 4. Reduction of spectral ghosts in EPSI data of human brain. Image intensity is proportional to the magnitudes of the true water peak (**a**) or the ghost peak (**b**). All images are displayed with an identical windowing setting. On the right are profiles of the image intensities through a horizontal line indicated by the arrows.

Table 2
Echo Shift Correction, Zero-Order Phase Correction, and Reduction of Spectral Ghost Peaks in EPSI Scans of Normal Human Brains at 1.5T*

Volunteer	Echo train shift in time (μs)	Phase correction on odd echoes (degree)	Ghost-to-true ratio	
			Uncorrected	Corrected
1	3.6	−0.34	0.099 (0.032, 0.204)	0.019 (0.012, 0.028)
2	6.0	−2.09	0.268 (0.093, 0.561)	0.041 (0.025, 0.065)
3	2.7	−3.46	0.095 (0.049, 0.191)	0.049 (0.034, 0.068)
4	6.7	−1.98	0.212 (0.077, 0.411)	0.035 (0.022, 0.065)
5	0.2	1.68	0.024 (0.013, 0.039)	0.027 (0.015, 0.041)
6	2.8	0.00	0.091 (0.049, 0.179)	0.047 (0.032, 0.065)
7	4.7	1.59	0.105 (0.041, 0.213)	0.036 (0.023, 0.054)
8	2.5	1.62	0.053 (0.029, 0.106)	0.028 (0.019, 0.040)

*The data presented are 50% (i.e., median) and 20%, 80% quantiles (in parenthesis) of the measurements obtained over an ROI covering most area of the brain.

therefore, the corrections are relatively large and lead to a remarkable decrease (sixfold) in the GTR. The original GTR is small in volunteer 5 and is not reduced after corrections.

The reduction of spectral ghosts in the EPSI data of human breast is illustrated in Fig. 5. In pixel 1 (which contains approximately equal amounts of fat and water tissues), the uncorrected spectrum clearly shows a ghost peak from the fat resonance and a weak ghost peak from the water resonance. In pixel 2 (which contains primarily fat), a single ghost peak is seen in the uncorrected spectrum. The magnitudes of the ghost peaks in these pixels are reduced to noise level after the corrections. Although spectra from many pixels in the breast, such as those shown in Fig. 5, were greatly improved by the correction, spectral ghosts in some pixels were not attenuated. Thus, the method in its current form is not as robust in the breast, where fat and water signals are present, as it is in the brain, where only the water peak is significant.

DISCUSSION

In the present work, a method for reducing spectral ghosts in EPSI of water and fat resonances is demonstrated. This method uses the EPSI data from the center of *k*-space to correct the relative misplacement and zero-order phase difference between the odd and even echoes. In contrast to the commonly used technique that separates the odd and even echoes for image reconstruction, the present method removes the ghost peaks without reducing the spectral bandwidth to half. The savings on spectral bandwidth is particularly important for high spatial resolution EPSI applications, where the spectral bandwidth is usually limited by a relatively long duration of each gradient echo.

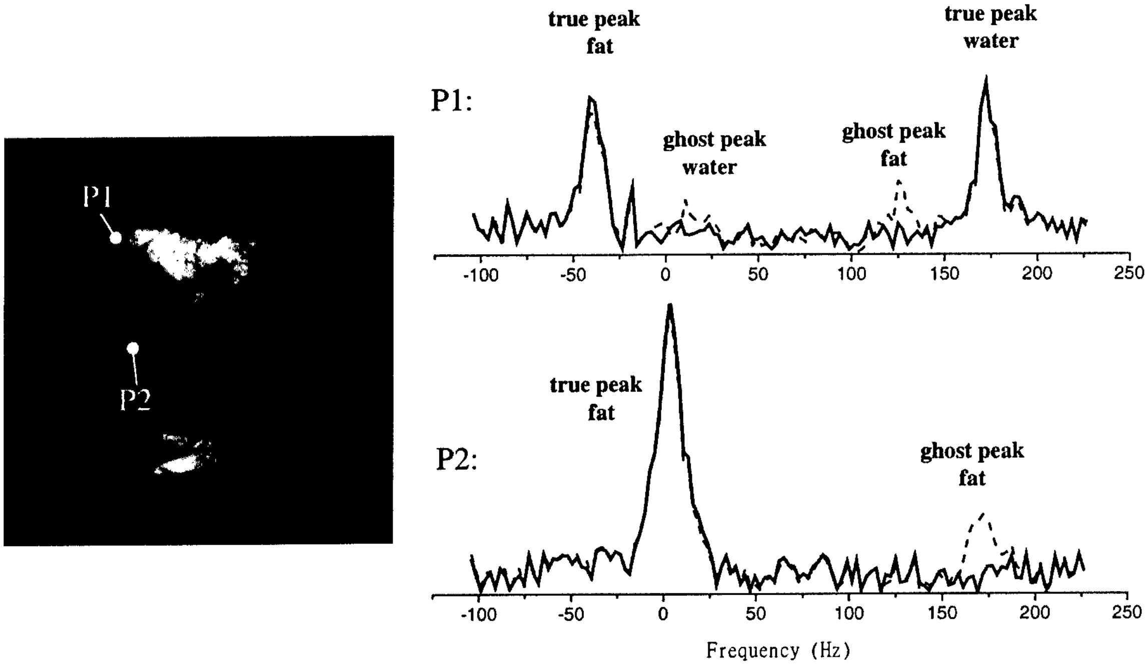

FIG. 5. Reduction of spectral ghosts in EPSI data of human breast. Left: An EPSI peak height image. Right: Spectra from two selected pixels (P1 and P2 in the image) calculated with (solid) and without (dash) echo shift and phase corrections.

Compared to other techniques that measure k-space trajectories to determine echo misalignments, the corrections are made during data processing, i.e., without the need for additional scans. This technique can be readily implemented with various EPSI sequences, such as 3D EPSI (9) and multishot EPSI (22).

EPSI data obtained without corrections display an interesting pattern of spectral ghost artifacts. The relative magnitudes of the ghost peaks vary significantly with respect to position in the echo-planar readout (x) direction, but do not vary as much in the phase-encoding direction (Figs. 3 and 4). The change in the ghost magnitude reflects a spatial variation in the extent of inconsistency between the odd and even echoes in the x direction, due to complicated echo shifts and distortions in the k_x direction. The inconsistency is severe at locations where large background gradients are present (e.g., near the edges of the brain in Fig. 4). Therefore, a global phase shift cannot by itself remove the artifacts from all pixels. In this work, the zero-order phase correction is used in combination with an echo shift correction. According to the Fourier theorems, an echo shift correction in the k_x direction is equivalent to a linear or first-order phase correction in the x direction. In essence, the echo shift correction is an extension of linear phase correction (17), which is widely used in EPI for removing image ghosts, to the task of removing spectral ghosts in EPSI. A nonlinear phase correction may better compensate for the effects of static field inhomogeneity on the data inconsistency, but it demands additional reference scans (17) and/or more sophisticated data processing techniques.

The zero-order phase correction is performed after the echo shift correction, i.e., after the linear phase discontinuity along the x direction is removed and only a residual constant phase discontinuity is left between the odd and even echoes. Despite its simplicity, the zero-order phase correction is effective: ghost intensity decreased from 0.28 to 0.027 in the water phantom experiments (see Table 1). The residual spectral ghosts are probably due to the fact that the phase evolution of the FID during each gradient echo is neglected in this study. During the echo-planar readout, the k_x-t-space is traversed in a zigzag fashion. Therefore, the sampling in time is not uniform for most of k-space points. This can generate spectral ghost artifacts. In the presence of a large off-resonance effect, it is necessary to make phase corrections for each k-space point (6,18). In our EPSI implementations for imaging water resonance in the phantom and human brains, the off-resonance effect is reasonably small. This is supported by the observation of the negligible magnitudes of residual ghost peaks after echo-shifting and phase correction (Fig. 4b). Further, the present method was also demonstrated to be useful for data acquired with interleaved EPSI. As with other multishot techniques (23,24), the signal varies from one acquisition to another. The zero-order phase correction provides a "self-navigated" way to trace and correct for the phase drift in the interleaved EPSI data.

The present method was developed for high-resolution functional and anatomic imaging of water and fat; therefore, it is more difficult to apply this method to water- and fat-suppressed EPSI of metabolites. First, the method may be sensitive to the noise in the data because of the low SNR nature of metabolite imaging. Second, multiple chemical shifts change the signal patterns in k-space. As a result, the determination of the k-space center using the CM technique may not be accurate. Third, the ghost from one true line may overlap another true line. In this case, it becomes difficult to minimize the ghost intensity using the method described above. Finally, a constant phase correction that minimizes the ghost from one true line may not reduce the ghosts from other lines. Despite these limitations, the correction still works well on the high-resolution EPSI data obtained from human breast (Fig. 5). With the current implementation, the correction is applied directly to the water/fat EPSI data. For metabolite EPSI, it might be possible to calculate the amount of correction from a reference scan in which water signal is not suppressed. Then the correction could be applied to the metabolite EPSI data, assuming that the inconsistency between the odd and even echoes is accurately measured with the reference scan. This hypothesis was not validated in this work, and requires further investigation.

It is interesting to note that significantly larger echo shift and phase corrections are necessary for the EPSI data obtained at 4.7 T compared to 1.5 T. Thus, the correction is more beneficial for the 4.7 T data. This is probably because of a relatively better performance of echo-planar gradients and relatively smaller background gradients on the lower field. The results from EPSI measurements may be used to characterize the system inaccuracies and eddy-current effects for EPI applications (25,26). For example, the oscillatory pattern of the CM of the gradient echoes is a sensitive indicator of system timing errors (Fig. 2a). In addition, the linear or nonlinear trend in the CM may be used to guide adjustment of shims to reduce background gradients.

In conclusion, a new method for reducing spectral ghost artifacts in EPSI of water and fat resonances is presented. This method uses an echo shift and zero-order phase correction to remove the inconsistency between the odd and even echoes. The spectral ghost artifacts are reduced significantly, as demonstrated in phantom and in vivo EPSI of water and fat resonances at 1.5 T and 4.7 T. A further reduction of spectral ghosts in EPSI is expected when this technique is combined with other reconstruction strategies, such as nonlinear phase correction (17) and interlaced Fourier transform (6,18).

REFERENCES

1. Mansfield P. Spatial mapping of the chemical shift in NMR. Magn Reson Med 1984;1:370–386.
2. Posse S, Tedeschi G, Risinger R, Ogg R, Le Bihan D. High speed 1H spectroscopic imaging in human brain by echo planar spatial-spectral encoding. Magn Reson Med 1995;33:34–40.
3. Posse S, Dager SR, Richards TL, Yuan C, Ogg R, Artru AA, Muller-Gartner HW, Hayes C. In vivo measurement of regional brain metabolic response to hyperventilation using magnetic resonance: proton echo planar spectroscopic imaging (PEPSI). Magn Reson Med 1997;37:858–865.
4. Matsui S, Sekihara K, Kohno H. Spatially resolved NMR spectroscopy using phase-modulated spin-echo-trains. J Magn Reson 1986;67:476–490.
5. Webb P, Spielman D, Macovski A. A fast spectroscopic imaging method using a blipped phase encode gradient. Magn Reson Med 1989;12:306–315.

6. Metzger G, Hu X. Application of the interlaced Fourier transform to echo-planar spectroscopic imaging. J Magn Reson 1997;125:166–170.
7. Hyder F, Renken R, Rothman DL. In vivo carbon-edited detection with proton echo-planar spectroscopic imaging (ICED PEPSI): [3,4-(13)CH(2)]glutamate/glutamine tomography in rat brain. Magn Reson Med 1999;42:997–1003.
8. Richards TL, Corina D, Serafini S, Steury K, Echelard DR, Dager SR, Marro K, Abbott RD, Maravilla KR, Berninger VW. Effects of a phonologically driven treatment for dyslexia on lactate levels measured by proton MR spectroscopic imaging. Am J Neuroradiol 2000;21.
9. Ebel A, Soher BJ, Maudsley AA. Assessment of 3D proton MR echo-planar spectroscopic imaging using automated spectral analysis. Magn Reson Med 2001;46:1072–1078.
10. Du W, Du YP, Bick U, Fan X, MacEneaney PM, Zamora MA, Medved M, Karcźmar GS. High spectral and spatial resolution MR imaging of breast—preliminary experience. Radiology 2002;224:577–585.
11. Kovar DA, Al-Hallaq HA, Zamora MA, River JN, Karczmar GS. Fast spectroscopic imaging of water and fat resonances to improve the quality of MR images. Acad Radiol 1998;5:269–275.
12. Kuroda K, Mulkern RV, Oshio K, Panych LP, Nakai T, Moriya T, Okuda S, Hynynen K, Joles FA. Temperature mapping using the water proton chemical shift: self-referenced method with echo-planar spectroscopic imaging. Magn Reson Med 2000;43:220–225.
13. Sarkar S, Heberlein K, Metzger GJ, Zhang X, Hu X. Applications of high-resolution echoplanar spectroscopic imaging for structural imaging. J Magn Reson Imaging 1999;10:1–7.
14. Yang QX, Demeure RJ, Dardzinski BJ, Arnold BW, Smith MB. Multiple echo frequency-domain image contrast: improved signal-to-noise ratio and T2 (T2*) weighting. Magn Reson Med 1999;41:423–428.
15. Barth M, Reichenbach JR, Venkatesan R, Moser E, Haacke EM. High-resolution, multiple gradient-echo functional MRI at 1.5 T. Magn Reson Imaging 1999;17:321–329.
16. Du YP, Du W, Uftring SJ, Fan X, Karczmar GS. fMRI with high spectral and spatial resolution echo-planar spectroscopic imaging at 1.5T. In: Proceedings of the 9th Annual Meeting of ISMRM, Glasgow, Scotland, 2001. p 1254.
17. Bruder H, Fischer H, Reinfelder HE, Schmitt F. Image reconstruction for echo planar imaging with nonequidistant *k*-space sampling. Magn Reson Med 1992;23:311–323.
18. Hanson LG, Schaumburg K, Paulson OB. Reconstruction strategy for echo planar spectroscopy and its application to partially undersampled imaging. Magn Reson Med 2000;44:412–417.
19. Takahashi A, Peters T. Compensation of multi-dimensional selective excitation pulses using measured *k*-space trajectories. Magn Reson Med 1995;34:446–456.
20. Haacke EM, Brown RW, Thompson MR, Venkatesan R. Magnetic resonance imaging: physical principles and sequence design. New York: John Wiley and Sons; 1999. p 846–848.
21. Jezzard P, Barnett AS, Pierpaoli C. Characterization of and correction for eddy current artifacts in echo planar diffusion imaging. Magn Reson Med 1998;39:801–812.
22. Tyszka JM, Mamelak AN. Volumetric multishot echo-planar spectroscopic imaging. Magn Reson Med 2001;46:219–227.
23. Hu X, Kim SG. Reduction of signal fluctuation in functional MRI using navigator echoes. Magn Reson Med 1994;31:495–503.
24. Glover GH, Lai S. Self-navigated spiral fMRI: interleaved vs. single-shot. Magn Reson Med 1998;39:361–368.
25. Chen NK, Wyrwicz AM. Correction for EPI distortions using multi-echo gradient-echo imaging. Magn Reson Med 1999;41:1206–1213.
26. Schmithorst VJ, Dardzinski BJ, Holland SK. Simultaneous correction of ghost and geometric distortion artifacts in EPI using a multiecho reference scan. IEEE Trans Med Imaging 2001;20:535–539.

APPENDIX 3

FOURIER COMPONENTS OF INHOMOGENEOUSLY BROADENED WATER RESONANCES IN BREAST

– A NEW SOURCE OF MRI CONTRAST

Milica Medved[1], Gillian Newstead[1], Xiaobing Fan[1], Weiliang Du[1], Yiping P. Du[3], Peter M. MacEneaney[1], Rita M. Culp, Frederick Kelcz[4], Olufunmilayo Obpade[2], Marta A. Zamora[1], Gregory Karczmar[1+]

Departments of [1]Radiology and [2]Medicine, University of Chicago; [3]Department of Psychiatry, University of Colorado Health Sciences Center; [4]Department of Radiology, University of Wisconsin at Madison.

[+]Address correspondence to:
Gregory S. Karczmar, Ph.D.
Department of Radiology, MC 2026
University of Chicago
5841 S. Maryland Ave.
Chicago, IL 60637
Tel: 773-702-0214 (o)
Fax: 773-702-1161
e-mail: gskarczm@midway.uchicago.edu

Running head: Fourier component images

ABSTRACT

High spectral and spatial resolution (HiSS) MR data were acquired at 1.5 Tesla using echo-planar spectroscopic imaging from patients with suspicious breast lesions. The water resonances in small voxels are inhomogenously broadened and often have distinct components. Images were calculated with intensity proportional to the Fourier components of the water resonance in each voxel at different offsets from the peak frequency. The results demonstrate that in breast, off-peak Fourier component images of water are qualitatively different from those derived from the peak height of the water resonance. These differences most likely reflect underlying anatomy or physiology. In conventional images, the superposition of the various Fourier components of the water signal may cause loss of detail. The synthesis of water Fourier component images from high spectral and spatial resolution data may provide a new form of contrast, and increase sensitivity to subvoxel physiology and anatomy.

Keywords: High spectral and spatial resolution MRI, MRI of breast, magnetic susceptibility imaging, subvoxel anatomy and physiology, image contrast

INTRODUCTION

The water resonance from small voxels in tissue is often inhomogeneously broadened, and sometimes contains multiple resolved components (1-5). These distinct components can be identified in water signal line shapes from single voxels in high spectral and spatial resolution (HiSS) images (5,6). In addition, distinct components can be identified based on spectrally inhomogeneous changes in the water resonance caused by changes in blood deoxyhemoglobin (1,7,8) or injected contrast agents (3,5,9,10). A priori arguments and experimental evidence suggest that the distinct components of the water resonance come from sub-voxelar, perhaps microscopic (3,5,9,10) environments that cannot be resolved by conventional imaging.

If the components of the water resonance represent specific subvoxel anatomic and physiologic features, it follows that images of these components may provide unique and potentially useful information. The purpose of this report is to demonstrate that HiSS imaging in human breast generates reproducible images of different Fourier components ('Fourier component images', or FCIs) of the water resonance from very small voxels, and that there are marked differences between different FCIs. The work described here does not attempt to correlate the information in FCIs with patient diagnosis, but rather to evaluate contrast in these novel images.

METHODS

Patient population

Data were acquired from women with suspicious breast lesions found on mammography. Standard clinical MRI scans were prescribed for these patients prior to biopsy primarily to determine whether there was disease extending beyond the focal abnormality identified on mammograms. A total of 13 patients was included in this study, of which 5 were confirmed by biopsy to have invasive ductal carcinoma (IDC), two to have ductal carcinoma in situ (DCIS), three to have IDC and DCIS, one to have IDC with sclerosing adenosis, and one to have fibroadenoma. In one patient, a lumpectomy scar was imaged.

Data acquisition

HiSS scans were incorporated into these standard exams, pre- and post-contrast agent administration. In addition, several volunteers with no breast abnormalities were scanned without the use of contrast agent. In studies of a limited number of patients (n = 4) with IDC, consecutive HiSS images were acquired 30-40 minutes post-contrast injection, when the changes due to contrast agent washout are negligible between the scans. Subjects were scanned under a protocol approved by the Institutional Review Board after informed consent had been obtained.

Images were obtained on a 1.5 Tesla clinical MRI scanner (General Electric) equipped with ECHO SPEED PLUS^{TM} gradients with maximum slew rate of 120 mT/m/s and maximum amplitude of 23 mT/m, using a dedicated, phased array breast coil. HiSS images were acquired from single selected slices using echo planar spectroscopic imaging (EPSI) (11,12). Immediately before the HiSS images were acquired, shimming was performed using the standard GE protocol, in which gradient echo images with several echoes are taken in all three planes, and phase differences between echoes are used to calculate adjustments to shim currents. The same shim and gain parameters were used to obtain both pre- and post-contrast HiSS images.

The EPSI sequence was composed of slice selection (slice thickness 4 mm) followed by phase encoding (256 phase encoding steps) and acquisition of 128 gradient echoes using trapezoidal gradient pulses with alternating polarity. A ‘crusher’ gradient was applied at the end of the echo train to eliminate artifacts due to residual transverse magnetization. Each gradient echo was sampled either at 256 (due to hardware limitations) or at 384 points (after a system upgrade). The data were digitized at a bandwidth of ± 62.5 kilohertz and the time between the centers of gradient echoes was approximately 3.0 ms. The proton free induction decay (FID) was sampled for a total of 384 ms and the time between excitations (TR) was 500 ms. The resulting data had in-plane spatial resolution of less than 1 mm (field-of-view of 24 cm or less) and spectral resolution of approximately 2.6 Hz. The spatial resolution was the same in both readout and phase encoding direction, resulting in a reduced field-of-view in the latter when a 384 by 256 image was acquired. The spectral bandwidth - approximately 333 Hz. - was sufficient to resolve the water and fat resonances, which are separated by approximately 220 Hz at 1.5 T. Both spectral and spatial resolutions were sufficient to avoid significant truncation artifacts. Sagittal slices were imaged with the readout gradient applied in the A/P direction to minimize artifacts due to respiratory and cardiac motion.

The shimming and data acquisition protocol was tested by imaging water phantoms containing 2 mM copper sulfate using the EPSI pulse sequence with the same parameters as those used for breast imaging (described above). The water resonance in all image voxels sampled was a symmetrical Lorentzian with line width of less than 2 Hz. No artifacts due to poor shimming or eddy currents were detected.

Data analysis and synthesis of images:

A 3D Fourier transform with respect to two k-space axes and the evolution of the FID (5,6,13-15) provided high resolution spectra of the water and fat resonances associated with each voxel in the image. The highest intensity spectral component was identified in each voxel, and the one in the voxel with highest signal was identified as either water or fat signal. Based on the frequency offset from this seed pixel, the highest peak in the neighboring voxel containing the highest signal was identified as either water or fat. Frequency foldback was accounted for, as well as the possibility of N/2 ghosting in the spectral dimension. This process was repeated using a region growing program, until all the voxels had been classified, and hence the fat and water frequency map obtained. This robust algorithm relies on the fact that there are no sharp macroscopic gradients within the breast, and is described in detail in our earlier publication. (15)

For examination of spectra from individual voxels, the water line from each voxel was phased by requiring that the integral of the imaginary spectrum in the narrow vicinity of the spectral peak equals zero. We found this to be equivalent to a requirement that the complex phase of the spectrum be zero at the peak frequency. However, the phasing algorithm in its present form sometimes results in errors. Therefore, magnitude spectra were used for image synthesis. Water signal peak height images provide a combination of T_1 and T_2* weighting. The T_2*-weighting was dominant in these data because the FID sampling time of 384 ms provided strong T_2* contrast, while the TR of 500 milliseconds provided only moderate T_1 weighting.

After the highest intensity spectral component was identified, images were synthesized with intensity proportional to the amplitude of the water spectrum at various offsets from the peak , in increments of 2.6 Hz (i.e. 1 frequency bin). These images are referred to in the following as FCIs – Fourier component images.

RESULTS

Figure 1 shows a post-contrast image of a breast with a high grade infiltrating ductal carcinoma (a), with the lesion outlined and enlarged in (b). In (b), the locations of eight representative voxels are indicated, and water spectra from these voxels are shown in (c)-(j). The solid and dashed lines correspond to two data sets acquired consecutively, 40 minutes post contrast. The underlying spectra acquired in the two scans are highly reproducible in intensity and structure. For example, water resonances with two resolvable components in one dataset show two very similar resolvable components in the second dataset.

The complexity of the water resonance in many voxels is reflected in images of the Fourier components of the water resonance. FCIs at 5 Hz to 30 Hz from the peak of the water resonance often contain features, well above noise level, that are different from images of the peak of the water resonance (at 0 Hz). In particular, FCI$_{-10}$ (the FCI generated at 10 Hz offset from the main peak) shows marked differences from FCI$_0$ more consistently then other FCIs. Figure 2 shows a T_1-weighted image (a), acquired pre-contrast injection in three patients with suspicious breast lesions (arrows). Pre-contrast FCIs at 0 Hz (FCI$_0$), (b) and -10 Hz (FCL$_{10}$) (c) from the peak of the water resonance are shown in detail for the 60 by 60 voxel area surrounding the lesion, as outlined in (a).

To highlight the variations in contrast among FCIs, the FCI_{-10}'s were subtracted from the corresponding FCI_0's, and the differences are shown in Figure 2d. Before subtraction, the average image intensity of each FCI within the region outlined in (a) was normalized to 1.0. As a result, the differences between the normalized images of the lesion and surrounding tissue emphasize differences in image contrast rather than image intensity. The difference images show coherent structures that are well above the noise level – which can be estimated from the variations in image intensity in regions where there is very little water signal. In particular, the dark structures correspond to features present in the off-zero FCI, but not in the peak height image (FCI_0), indicating a non-Lorentzian water line shape. Some structures are elongated and appear to be blood vessels (rows 1, 3, 4 in particular). In addition, there are frequent 'black dots' in and near lesions, which may come from blood vessels perpendicular to the image slices. The blood vessels may have a different relative intensity in FCI_0 and $FCI_{-10,}$ due to the magnetic susceptibility of deoxyhemoglobin.

DISCUSSION

Previous work demonstrated that high spectral and spatial resolution imaging provides strong T_2* contrast while showing excellent anatomic detail relative to conventional MRI (5,6,14,16,17). The present work suggests that Fourier component imaging can be an additional, novel source of contrast in HiSS data. The preliminary results presented here demonstrate that FCIs at different offsets from the peak of the water resonance differ markedly. This would not be the case if the water resonance in each voxel was a homogeneously broadened Lorentzian. It is not known at present whether the same features seen in FCIs could also be emphasized using more commonly used contrast mechanisms, i.e. T_1, T_2, T_2*, diffusion, or magnetization transfer-weighting. If the FCIs provide an independent contrast mechanism, HiSS MRI could be combined with other methods for contrast enhancement to increase the amount of information offered by MRI. The present results do not indicate whether Fourier component images are clinically useful, as there is no evidence as yet that FCIs of cancers are different from FCIs of benign lesions. More work is required to optimize acquisition and processing of FCI images before clinical applications can be evaluated.

Motion artifacts are a potential source of error in the calculations of FCI's because they can cause contamination of the water spectrum in each voxel by water signals from nearby voxels. Since the contaminating signal may be at a different frequency from the local water resonance, this could lead to broadening of the water resonance, and in some cases might appear as an off-resonance component. However, in our experience, this artifact is easily observable in the phase encoding direction in water peak height (FCI_0) images, and is of much lower signal intensity than the main image. The HiSS images presented here do not show any such aliasing, and Fig.1c shows that resolved water components are of comparable intensity. Therefore, the water components we detect are unlikely to result from motion artifacts.

It is not likely that the spectrally inhomogeneous broadening could be caused by imperfect shimming. In the small voxels used in HiSS MRI, the macroscopic B_0 gradients across each voxel are small and, to a very good approximation, linear, and are likely to produce modest broadening of the water resonance, but no 'peak splitting'. B_0 generally varies slowly and smoothly within the breast, and we do not observe large gradients in the vicinity of voxels with complex water signals. Finally, the Fourier component images in Figure 3 often show discrete, elongated structures, that have the appearance of blood vessels, which would not be seen if the water line structure resulted simply from poor shimming. It is more likely that the peak splitting and inhomogenous broadening are the result of sub-voxelar variations in magnetic susceptibility. For example, at 1.5 Tesla, deoxyhemoglobin in a capillary can cause a gradient of 30 Hz over a distance of 5 microns, which is equivalent to ~15 Gauss/cm, and hemosiderin may cause even larger gradients. It is plausible that each FCI may represent a discrete subvoxelar environment with characteristic magnetic susceptibility – analogous to the chemical shift imaging of metabolites where images of the signal at a specific frequency produce images of a specific metabolite. (18,19) Thus, HiSS MR may be able to resolve subvoxelar environments, inaccessible via conventional imaging, potentially increasing sensitivity to subvoxelar anatomy and physiology. This hypothesis must be tested by direct correlation of Fourier component images with histology.

In conclusion, we show that the various Fourier components of the water resonances in small voxels can produce images with differing contrast and anatomic detail. This contrast is likely the result of sub-voxelar breast anatomy or physiology, a contrast mechanism that likely can not be duplicated using other methods. The present results do not identify the sources of contrast in FCI images, and do not indicate whether Fourier component images are clinically useful However, the FCIs shown here reveal new features that could potentially aid the evaluation of suspicious breast lesions.

ACKNOWLEDGEMENTS

This work was funded by the NCI (1RO1CA76476 and 1RO1CA78803), the Army Breast Cancer Research Program (BC981147), and the Paul C. Hodges Society. GSK is grateful to Dr. Alan Koretsky and Dr. Charles Springer for helpful advice, and to the American Cancer Society volunteers of Will and Grundy Counties, in Illinois, for their enthusiastic support.

REFERENCES

1. Al-Hallaq HA, Fan X, Zamora M, River JN, Moulder JE, Karczmar GS. Spectrally inhomogeneous BOLD contrast changes detected in rodent tumors with high spectral and spatial resolution MRI. NMR Biomed 2002;15(1):28-36.
2. Karczmar GS, Fan X, Al-Hallaq HA, Zamora M, River JN, Rinker-Schaeffer C, Zaucha M, Tarlo K, Kellar K. Uptake of a superparamagnetic contrast agent imaged by MR with high spectral and spatial resolution. Magn Reson Med 2000;43:633-639.
3. Karczmar GS, Fan X, Al-Hallaq H, River JN, Tarlo K, Kellar KE, Zamora M, Rinker-Schaeffer C, Lipton MJ. Functional and anatomic imaging of tumor vasculature: high-resolution MR spectroscopic imaging combined with a superparamagnetic contrast agent. Acad Radiol 2002;9 Suppl 1:S115-118.
4. Karczmar GS, Du W, Medved M, Bick U, MacEneany P, Du YP, Fan X, Zamora M, Lipton M. Spectrally inhomogeneous effects of contrast agents in breast lesion detected by high spectral and spatial resolution MRI. Acad Radiol 2002;9 Suppl 2:S352-354.
5. Du W, Du YP, Bick U, Fan X, MacEneaney PM, Zamora MA, Medved M, Karczmar GS. Breast MR Imaging with High Spectral and Spatial Resolutions: Preliminary Experience. Radiology 2002;224(2):577-585.
6. Kovar DA, Al-Hallaq HA, Zamora MA, River JN, Karczmar GS. Fast spectroscopic imaging of water and fat resonances to improve the quality of MR images. Acad Radiol 1998;5(4):269-275.
7. Al-Hallaq HA, Zamora M, River JN, Karczmar GS. MR correctly predicts the relative effect of two tumor oxygenating agents on hypoxic fraction in rodent BA1112 tumors. 1999; Philadelphia. International Society for Magnetic Resonance in Medicine. p 496.
8. Oikawa H, Al-Hallaq HA, Lewis MZ, River JN, Kovar DA, Karczmar GS. Spectroscopic imaging of the water resonance with short repetition time to study tumor response to hyperoxia. Magn Reson Med 1997;38(1):27-32.

9. Naritomi H, Kanashiro M, Sasaki M, Kuribayashi Y, Sawada T. In vivo measurements of intra- and extracellular Na+ and water in the brain and muscle by nuclear magnetic resonance spectroscopy with shift reagent. Biophys J 1987;52(4):611-616.

10. Zhong K, Li X, Shachar-Hill Y, Picart F, Wishnia A, Springer CSJ. Magnetic susceptibility shift selected imaging (MESSI) and localized (1)H(2)O spectroscopy in living plant tissues. NMR Biomed 2000;13(7):392-397.

11. Doyle M, Mansfield P. Chemical shift imaging: a hybrid approach. Magn Reson Med 1987;5:255-261.

12. Mansfield P. Spatial mapping of the chemical shift in NMR. Magn Reson Med 1984;1:370-386.

13. Fan X, Du W, MacEneaney P, Zamora M, Karczmar G. Structure of the water resonance in small voxels in rat brain detected with high spectral and spatial resolution MRI. J Magn Reson Imaging 2002;16(5):547-552.

14. Kovar DA, Karczmar GS. Fast spectroscopic imaging of water and fat proton resonances improves image contrast and signal-to-noise ratio. 1997; Vancouver, Canada. p 1834.

15. Medved M, Du W, Zamora MA, Fan X, Olopade OI, MacEneaney PM, Newstead G, Karczmar GS. The effect of varying spectral resolution on the quality of HiSS MR images of the breast. J of Magn Reson Imaging 2003;18(4):442-448.

16. Kuperman V, River JN, Karczmar GS. High resolution spectroscopic images of tumors. 1995; Nice, France. International Society of Magnetic Resonance in Medicine.

17. Sarkar S, Heberlein K, Metzger GJ, Zhang X, Hu X. Applications of high-resolution echoplanar spectroscopic imaging for structural imaging. J Magn Reson Imaging 1999;10(1):1-7.

18. Brown TR, Kincaid BM, Ugurbil K. NMR chemical shift imaging in three dimensions. Proc Natl Acad Sci U S A 1982;79(11):3523-3526.

19. Maudsley AA, Hilal SK, Perman WH, Simon HE. Spatially Resolved High Resolution Spectroscopy by "Four-Dimensional" NMR. Journal of Magnetic Resonance 1983;51:147-152.

FIGURE LEGENDS

Figure 1: (a) A sagittal, water peak height HiSS image for a patient with a high grade invasive ductal carcinoma lesion is shown. (b) The lesion, outlined in (a), is enlarged to show the position of voxels for which the water spectra are shown in (c-j). (c)-(j): Spectra from two repeated measurements are shown for comparison (solid and dashed lines), for the eight voxels noted in (b).

Figure 2: A pre-contrast T1-weighted (a) image, is shown for 3 patients with breast lesions (diagnosis, top to bottom: intraductal and invasive ductal adenocarcinoma, infiltrating ductal carcinoma, fibroadenoma). Pre-contrast FCIs for 0 Hz (b) and +10 Hz (c), as well as their difference (d) are also shown, for the region outlined in (a). Arrows in (d) point to new features that appear in off-zero FCIs.

FIGURES:

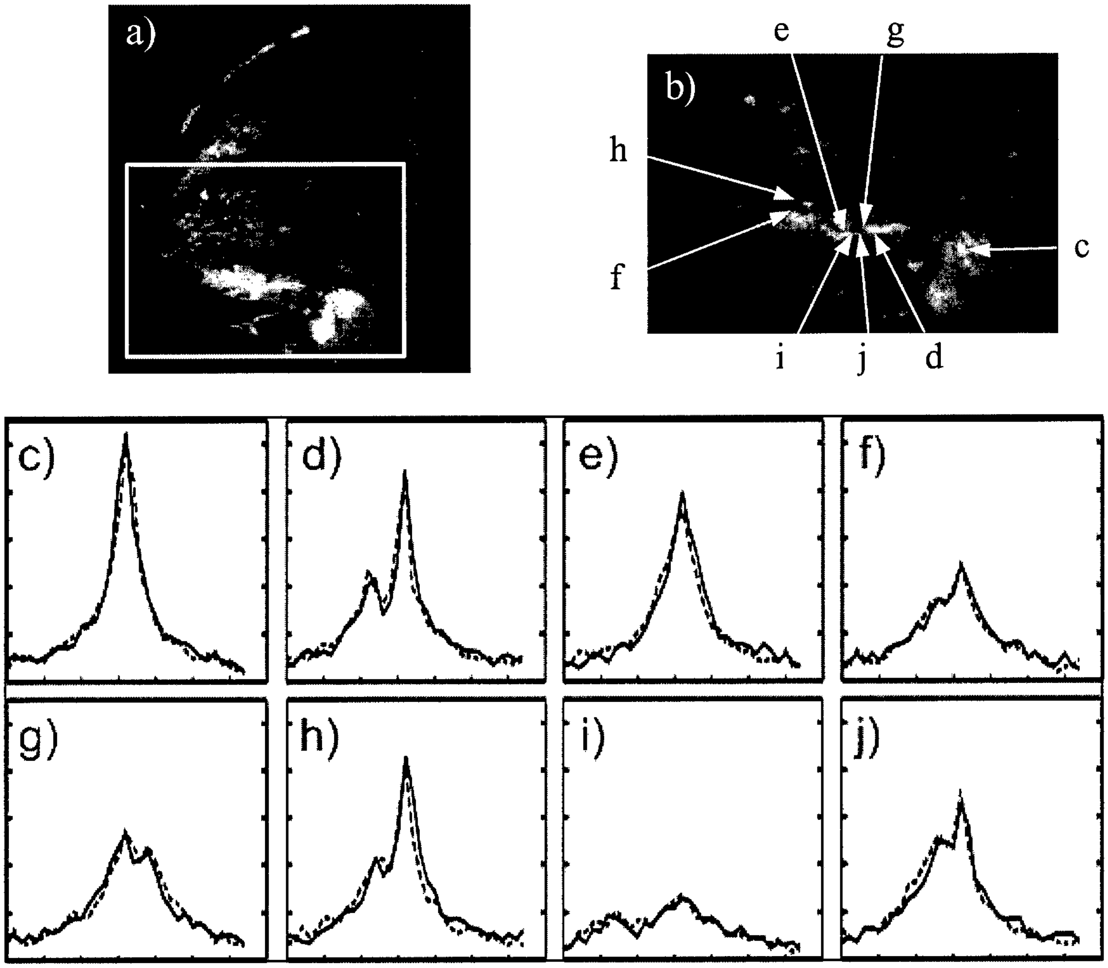

Figure 1: (a) A sagittal, water peak height HiSS image for a patient with a high grade invasive ductal carcinoma lesion is shown. (b) The lesion, outlined in (a), is enlarged to show the position of voxels for which the water spectra are shown in (c-j). (c)-(j): Spectra from two repeated measurements are shown for comparison (solid and dashed lines), for the eight voxels noted in (b).

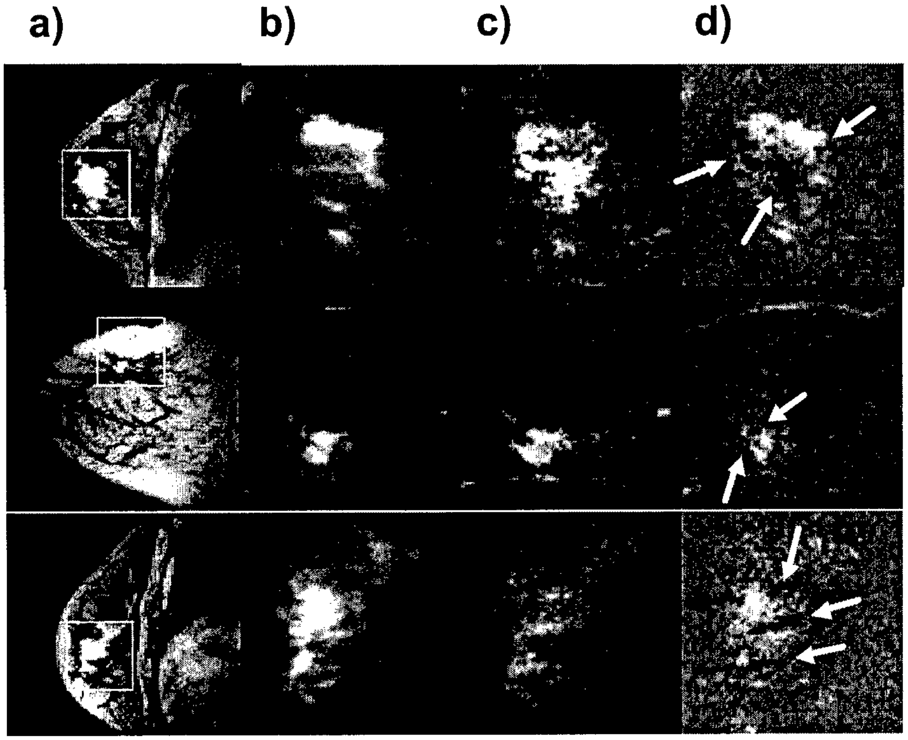

Figure 2: A pre-contrast T1-weighted (a) image, is shown for 3 patients with breast lesions (diagnosis, top to bottom: intraductal and invasive ductal adenocarcinoma, infiltrating ductal carcinoma, fibroadenoma). Pre-contrast FCIs for 0 Hz (b) and +10 Hz (c), as well as their difference (d) are also shown, for the region outlined in (a). Arrows in (d) point to new features which appear in off-zero FCIs.